Geophysical Research Letters

RESEARCH LETTER
10.1029/2024GL112069

Mantle Exhumation and Post-Rift Magmatism at an Oblique Magma-Poor Continental Margin

Jie Chen[1,2,3], Sylvie Leroy[2], Louise Watremez[4], and Adam H. Robinson[5]

[1]Université Paris Cité, Institut de physique du globe de Paris, Paris, France, [2]Sorbonne Université, CNRS-INSU, Institut des Sciences de la Terre Paris, Paris, France, [3]Laboratoire de Géologie, Ecole Normale Supérieure, PSL Research University, Paris, France, [4]Université de Lille, CNRS, Université Littoral Côte d'Opale, IRD, UMR, Laboratoire d'Océanologie et de Géosciences, Lille, France, [5]School of Ocean and Earth Science, University of Southampton, Southampton, UK

Abstract Continental breakup is a fundamental tectonic process, which leads to seafloor spreading and the generation of oceanic crust. However, the current understanding of continental margins, based largely on 2-D seismic transects, is inadequate to capture the spatial complexity of crustal evolution. Here we present a 3-D seismic velocity model through a young, magma-poor margin at the north-eastern Gulf of Aden. Our results highlight the 45° obliquity between the strike of crustal thinning and extension direction, which is accommodated by two transfer zones during the formation of the Continent-Ocean Transition (COT). This obliquity causes the margin to be segmented, which predates seafloor spreading. Along strike, we find a progressive eastward crustal thinning from 13 to 5 km, corresponding to a V-shaped COT. This eastward variation is characterized by (a) an eastward increase of mantle exhumation due to detachment faulting, and (b) post-rift magmatism emplaced onto serpentinized mantle in the west.

Plain Language Summary This study explores how continents break apart, focusing on the north-eastern Gulf of Aden, where the continental crust stretched and thinned to form a new ocean. Using 3-D seismic data, we examined changes in crustal thickness and structure during this process. We found a 45° angle (obliquity) between directions of crustal thinning and extension, a feature that significantly impacts the pattern of seafloor spreading as the ocean grows. In the region known as the Continent-Ocean Transition (COT), the crust progressively thins from 13 to 5 km toward the east. By combining these observations with earlier studies of magnetism and heat flow, we identified two distinct stages of crustal thinning. First, the mantle rock beneath the crust is exposed through faulting, especially in the east. Later, volcanic activity in the west adds new material onto the stretched mantle. This study shows how different processes, both during and after continental breakup, shape the crust, improving our understanding of this fundamental global tectonic process.

Key Points:

- 3-D crustal structure at a magma-poor continental margin of the north-eastern Gulf of Aden is imaged by a seismic velocity tomography
- A 45° obliquity of crustal thinning is observed, causing margin segmentation and inherited by ongoing seafloor spreading
- Mantle exhumation by detachment faults and post-rift magmatism shape margin crusts and build a V-shaped Continent-Ocean Transition

Supporting Information:

Supporting Information may be found in the online version of this article.

Correspondence to:

J. Chen,
chen@geologie.ens.fr

Citation:

Chen, J., Leroy, S., Watremez, L., & Robinson, A. H. (2025). Mantle exhumation and post-rift magmatism at an oblique magma-poor continental margin. *Geophysical Research Letters*, *52*, e2024GL112069. https://doi.org/10.1029/2024GL112069

Received 20 AUG 2024
Accepted 1 FEB 2025

Author Contributions:

Conceptualization: Jie Chen, Sylvie Leroy, Louise Watremez
Data curation: Sylvie Leroy, Louise Watremez
Formal analysis: Jie Chen, Louise Watremez
Funding acquisition: Sylvie Leroy
Investigation: Sylvie Leroy, Louise Watremez
Methodology: Jie Chen, Louise Watremez, Adam H. Robinson
Project administration: Sylvie Leroy
Software: Jie Chen, Louise Watremez, Adam H. Robinson
Supervision: Sylvie Leroy, Louise Watremez

1. Introduction

Passive continental margins are crucial for understanding the onset of the seafloor spreading at mid-ocean ridges and the evolution from continental to oceanic crust. Two endmembers of margin types—magma-rich and magma-poor—have been defined based on the degree of magmatism in syn-rift processes (Brune et al., 2023; Geoffroy, 2005; Minshull, 2009). At magma-rich margins, syn-rift magmatism produces a thick igneous crust at the Continent-Ocean Transition (COT), usually related to mantle plumes (Geoffroy, 2005; White & Smith, 2009). Such margins may be found at the Paraná-Etendeka igneous province of the South Atlantic margin (Sauter et al., 2023) and the western Gulf of Aden (Leroy et al., 2012; Tard et al., 1991). At magma-poor margins, for example, the Iberia-Newfoundland conjugate margin (Péron-Pinvidic & Manatschal, 2009; Van Avendonk et al., 2006) and the eastern Gulf of Aden (Leroy et al., 2012), serpentinized mantle is exhumed at the COT through detachment faults (Lavier & Manatschal, 2006; Minshull, 2009; Pérez-Gussinyé & Reston, 2001; Tucholke et al., 2007). However, in addition to syn-rift magmatic variations, continental margins are also subject to various processes, such as (a) margin segmentation and oblique extension (Leroy, Lucazeau, et al., 2010; Lizarralde et al., 2007; Zhang et al., 2023), (b) post-rift volcanism (Lucazeau et al., 2008; Pallister et al., 2010), and (c) subsidence and sedimentation (Winterer & Bosellini, 1981). Understanding such spatial variability along and across continental margins remains a fundamental research objective in plate tectonics, which necessitates 3-D seismic volumes (Boddupalli et al., 2022; Zhang et al., 2023).

Validation: Sylvie Leroy, Louise Watremez
Writing – original draft: Jie Chen
Writing – review & editing: Sylvie Leroy, Louise Watremez, Adam H. Robinson

The Gulf of Aden is a young continental rifted margin (rifting at 34–17.6 Ma ago) (Figure 1), which shows a magma-rich margin structure toward the west, related to the Afar mantle plume, and a magma-poor margin structure to the east, with a possible zone of exhumed mantle (d'Acremont et al., 2005; Leroy et al., 2012; Leroy, Lucazeau, et al., 2010; Nonn et al., 2017, 2019; Tard et al., 1991). The oblique rifting (40–60° relative to the extension direction) leads to segmentation and fracture zones at the margin, which is covered by thin sediments and scattered post-rift volcanism (Figure 1) (Autin et al., 2010; d'Acremont et al., 2010; Fournier et al., 2004; Korostelev et al., 2015; Leroy, Lucazeau, et al., 2010; Watremez et al., 2011). This provides a unique opportunity to study spatial variations in the tectonic evolution of continental margins during both syn-rift and post-rift processes. Here we report tomographic P-wave velocity (Vp) observations from an active source, onshore-offshore, three-dimensional (3-D) wide angle seismic experiment (data acquisition in Text S1 in Supporting Information S1) conducted over three second-order margin segments (Seg-1, Seg-2, and Seg-3, also named as Ashawq-Salalah, Taqah, and Mirbat segments in previous studies (Leroy, Lucazeau, et al., 2010)), at the north-eastern Gulf of Aden between Alula-Fartak (AFFZ) and Socotra-Hadbeen (SHFZ) Fracture Zones (Figure 1). These three segments all display a magma-poor margin structure, and are offset by two transfer zones, which show an eastward widening of a V-shape COT (Autin et al., 2010; Leroy, Lucazeau, et al., 2010) (Figure 1c). Despite no evidence of syn-rift volcanism (Autin et al., 2010; Leroy et al., 2012; Leroy, Lucazeau, et al., 2010), post-rift volcanism has been discovered over the western Seg-1, probably occurring until as recently as ∼100 ka ago, as indicated by an elevated heat flow values observed on the present-day seafloor (Leroy, d'Acremont et al., 2010; Lucazeau et al., 2008, 2009, 2010).

2. Results and Discussion

The First Arrival Seismic Tomography (FAST) software (Zelt & Barton, 1998) is used to compute the 3-D Vp model (data processing in Text S1). The final 3-D Vp model covers an area of 5–165 km and 5–115 km in X (east-west) and Y (south-north) directions, respectively (Figures 2 and 3), with a good spatial resolution at Z (depth below sea level) ≤12 km, where features larger than 10 km near the COT can be well imaged without notable smearing or distortion (spatial resolution in Figures S8 and S11E in Supporting Information S1 and checkerboard test in Figures S13 and S14 in Supporting Information S1).

By comparing coincident 2-D layered models that include a Moho interface (determined using reflected PmP phases) (Leroy, Lucazeau, et al., 2010; Watremez et al., 2011), we find that the 7.5 km/s iso-velocity contour in our 3-D model is a good proxy of the Moho location at the COT and oceanic crusts (Text S1 and Figure S15 in Supporting Information S1). The total crustal thickness, measured between the oceanic basement or the land's surface and the 7.5 km/s iso-velocity contour, decreases from >20 km to 13-5 km from continental to oceanic crusts within ∼60 km (Figure 2b). The 6.4 km/s iso-velocity contour is used to distinguish the boundary between the upper and lower crust, with the upper crust in the COT and oceanic crust domains approximately limited above a vertical Vp gradient of 0.5/s (Figure S11B in Supporting Information S1).

Vertical 1-D Vp profiles of the continental crust (Panels A in Figure S12 in Supporting Information S1) are consistent with the continental velocity structure of the north-eastern Gulf of Aden derived from previous 2-D seismic Vp tomography (Leroy, Lucazeau, et al., 2010; Watremez et al., 2011). The map of stretching factor β (Figure 2c), calculated as the ratio of the maximum, un-thinned, continental crustal thickness (36.6 km inferred by receiver functions (Tiberi et al., 2007)) to the total crustal thickness, indicates that the study area is a typical magma-poor margin with a β factor of mostly >4 within the COT (Watremez et al., 2011).

Tomography models, showing velocities increasing from 1.5 km/s in water to over 8 km/s in the mantle, are used to interpret the nature of crustal and uppermost mantle materials (Dunn et al., 2005; Minshull, 2009; White et al., 2008). We define (a) a layer between the 6.0 and 6.4 km/s iso-velocities as the middle crust (Figure 2d) to delineate the boundary between continental and oceanic crusts, and (b) a layer between the 7.0 and 7.5 km/s iso-velocities as intermediate velocities (Figure 2e), which are typically too fast for crustal material (Carlson & Miller, 2004) and too slow for the unaltered mantle (Christensen, 2004). Depth uncertainties of iso-velocities at 6.0, 6.4, 7.0, and 7.5 km/s are shown in Figure S10 in Supporting Information S1.

Serpentinization can lower the Vp of mantle rocks from 8 to 5 km/s (Christensen, 2004), overlapping igneous crustal Vp values, which creates ambiguity in distinguishing between igneous crust and serpentinized mantle. Here we use vertical Vp gradient as a proxy to define the intermediate layer (Watremez et al., 2011), whether it consists of: (a) an igneous body at the base of the crust with a nearly-uniform composition (low velocity

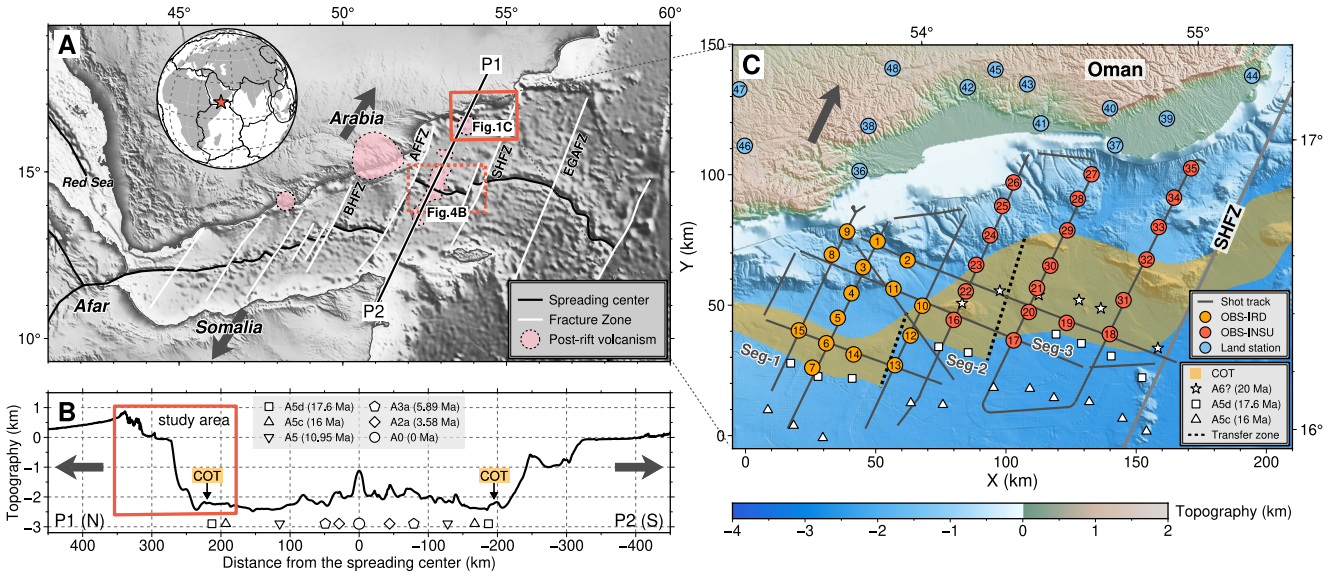

Figure 1. Tectonic setting of the Gulf of Aden and the 3-D seismic refraction experiment. Gray arrows show the extension direction. (a) Shaded topographic map. Pink areas indicate post-rift volcanism (Korostelev et al., 2015; Leroy, d'Acremont et al., 2010; Lucazeau et al., 2010). Black and white lines mark spreading centers and fracture zones, respectively. The inset hemisphere shows the location of the study area. (b) Topographic cross-section along P1–P2 located in panel (a). See legend for symbols of magnetic anomalies (d'Acremont et al., 2006; Leroy et al., 2004). (c) Combined onshore-offshore seismic survey during the Encens cruise in 2006 (Leroy, 2006), conducted over three second-order margin segments (Seg-1, Seg-2, and Seg-3) at the north-eastern Gulf of Aden. See legend for symbols of OBSs, land stations, and wide-angle seismic shot tracks. OBSs were provided by IRD and INSU institutions. Orange shaded area indicates the extent of the Continent-Ocean Transition (COT), inferred from previous geophysical observations, that is, seismic reflection/refraction, magnetism, and heat flow (Autin et al., 2010; d'Acremont et al., 2006; Leroy et al., 2004; Leroy, Lucazeau, et al., 2010; Lucazeau et al., 2008). Fracture zones: Socotra-Hadbeen (SHFZ), Alula-Fartak (AFFZ), Bosaso-Hami (BHFZ), and Eastern Gulf of Aden (EGAFZ).

gradients), (b) a transition from partly serpentinized exhumed mantle material (<30% serpentinization according to Christensen (2004)) to unaltered mantle (higher velocity gradients), or (c) the Mohorovičić discontinuity, marking the sharp boundary between the crust and mantle (no intermediate layer with highest velocity gradients).

2.1. Oblique Crustal Thinning

Oblique crustal thinning is observed within Seg-1 and Seg-2, at an angle of ~45° relative to the extension direction, roughly perpendicular to the coastline (Figure 2). Dense contours of the total crustal thickness near the northern limit of the COT are parallel to the coastline, for example, the 10 km contour (Figure 2b). The middle crust (Figure 2d) and the intermediate velocities (Figure 2e) also show a clear boundary with an oblique strike between the continental and COT crusts, which are both thicker toward the continental domain. The depth slice of $Z = 12$ km (~10 km below seafloor) shows that the 7.5 km/s iso-velocity shallows toward the oceanic domain, also following a trend parallel to the coastline (Figure 2f).

The obliquity (45°) between the strike of crustal thinning and extension direction at Seg-1 and Seg-2 (Figure 2) is consistent with the regional obliquity of the northern margin of the Gulf of Aden (Fournier et al., 2004), relative to the direction of seafloor spreading. It also aligns with the trend of a high Residual Mantle Bouguer gravity Anomaly (RMBA) near the COT (d'Acremont et al., 2010) (Figure S9D in Supporting Information S1). However, the second-order segmentation, related to the nascent spreading center near the southern limit of the COT, displays a strike almost perpendicular to the extension direction (Figure 1c). This is corroborated by the first magnetic anomaly, that is, A5d (17.6 Ma; Figure 1c), which indicates the formation of the earliest oceanic crust in this region (d'Acremont et al., 2006, 2010; Leroy et al., 2004). Such segmentation also pre-existed for the ongoing seafloor spreading, which then shows its own distinct segmentation processes (Figures 4a and 4b). We, therefore, propose that during the formation of the COT, the regional extension obliquity was accommodated by the lateral offset of two second-order transfer zones that correspond to locally thin crusts (Figure 2b). The margin segments were cut to be nearly perpendicular to the extension direction, probably due to the thinning of the continental mantle lithosphere (Duclaux et al., 2020). Such a mechanism could also be applicable to slow and ultraslow spreading mid-ocean ridges, such as the Southwest Indian Ridge (SWIR), where regional spreading obliquity is

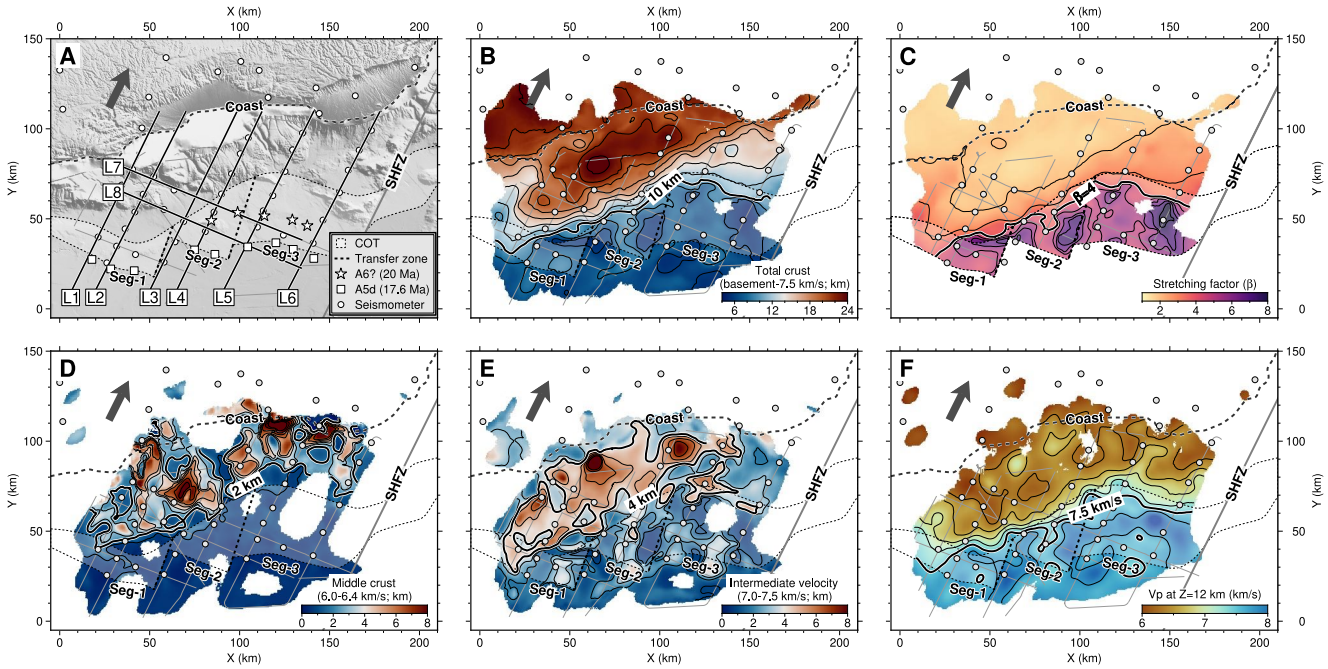

Figure 2. Map view of the final 3-D Vp model. White masks correspond to areas without ray coverage. Gray arrows show the extension direction. (a) Shaped topographic map. See legend for the COT, transfer zones, magnetic anomalies, and seismometers. Solid lines (L1–L8) oriented parallel and perpendicular to the extension direction are the locations of vertical slices in Figure 3. (b) Total crustal thickness, calculated between the basement top and the 7.5 km/s iso-velocity. Contour interval is 2 km. (c) Stretching factor (β), calculated as the ratio of the maximum continental crustal thickness (36.6 km inferred by receiver function (Tiberi et al., 2007)) and the total crustal thickness (b). Oceanic crust is excluded. Contour interval is 1. (d) Middle crustal thickness, calculated between the 6.0 and 6.4 km/s iso-velocities, contoured at 1 km intervals. (e) Thickness of the intermediate velocity layer, calculated between the 7.0 and 7.5 km/s iso-velocities. Contour interval is 1 km. (f) Depth slice at $Z = 12$ km, within the well-resolved part of the 3-D Vp model at a resolution of <10 km (Figure S8D in Supporting Information S1), contoured at 0.3 km/s intervals.

inherited from the initial rifting system and then accommodated by ridge-perpendicular transform faults and ridge-oblique non-transform discontinuities that bound nearly-orthogonal ridge segments (Cannat et al., 1999; Chen et al., 2023; Sauter et al., 2001).

2.2. Post-Rift Magmatism Emplacing Onto Exhumed Mantle

Along the COT, our 3-D seismic velocity volume shows a high spatial variation of the crustal structure across the three margin segments. From west to east, the seismic crustal thickness decreases from 13 to 5 km, coinciding with an eastward widening (from 15 to 50 km) of the V-shaped COT (Figure 2). At the western Seg-1 (94 km long), the presence of a >10 km-thick crust (Figure 2b) and a >4 km-thick intermediate layer (Figure 2f) at the COT is unexpected for a magma-poor rifted margin (Watremez et al., 2011), particularly the 13 km-thick crust (Figures 3A-1) with a low (<0.2/s) vertical Vp gradient in the intermediate layer (Figure S11B-1 in Supporting Information S1) at the profile L1. In addition, an extremely high heat flow (~900 mW/m^2) and a series of volcanic-flow reflectors have been observed over a seamount at the profile L2, indicating that post-rift magmatism may be responsible for the crustal thickening (Autin et al., 2010; Leroy, d'Acremont et al., 2010; Lucazeau et al., 2010). Because the upper crustal thickness (basement to 6.4 km/s iso-velocity) and the crustal thickness without the intermediate velocities (basement to 7.0 km/s iso-velocity) are relatively uniform along the COT (Figures S9A and S9C in Supporting Information S1), this post-rift magmatism dominantly appears to take the form of underplated materials and/or magma-intruded lower crust (Figure 4c), which mainly contributes to the low-gradient intermediate velocity (between the 7.0 and 7.5 km/s iso-velocities; Figure 2e in Supporting Information S1).

Two stages of rifting have been proposed for the COT formation in the western part of Seg-1 (Autin et al., 2010; Leroy, Lucazeau, et al., 2010; Watremez et al., 2011): (a) mantle exhumation along detachment faults, followed by (b) post-rift magmatism soon after the continental breakup and/or during early seafloor spreading. Previous studies suggest that the evidence of the exhumed mantle during stage-1 may have been fully overprinted by post-

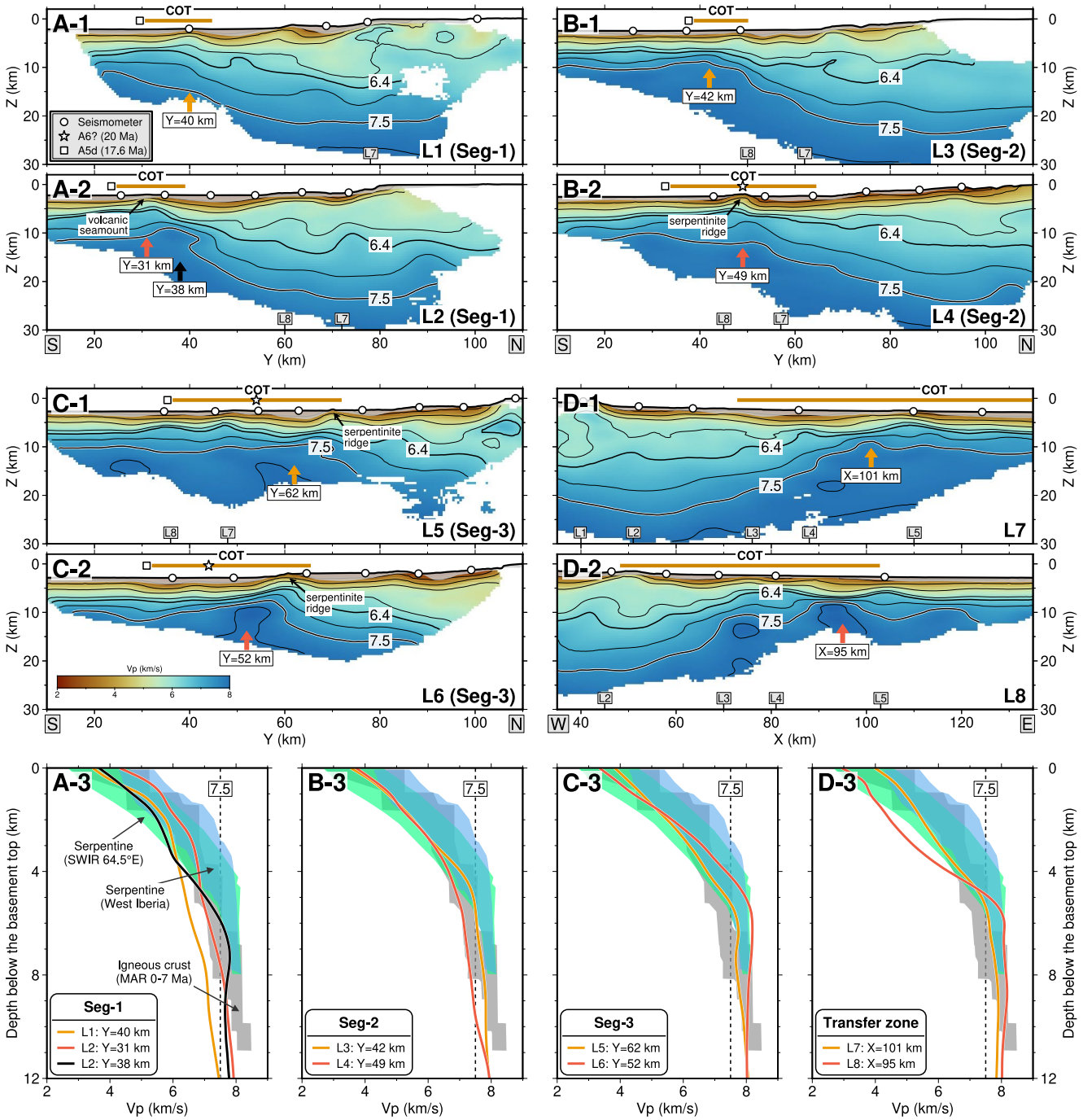

Figure 3. Vertical Vp slices and 1-D profiles along acquisition lines. Profile locations oriented parallel (L1–L6) and perpendicular (L7–L8) to the extension direction are shown in Figure 2a. Color bar of Vp is shown in C-2. (A-1) and (A-2) Profiles L1 and L2 across the western Seg-1. (B-1) and (B-2) Profiles L3 and L4 across the central Seg-2. (C-1) and (C-2) Profiles L5 and L6 across the eastern Seg-3. (D-1) and (D-2) Profiles L7 and L8 across transfer zones. (A-3) - (D-3) 1-D Vp profiles, extracted from corresponding segments and transfer zones. Gray envelope represents the igneous crust at the age of 0–7 Ma of the Mid-Atlantic Ridge (MAR) (White et al., 1992). Green and blue envelopes represent serpentinized mantle of the ultraslow-spreading SWIR 64.5°E (Corbalán et al., 2021; Momoh et al., 2017) and the magma-poor West Iberia rifted margin (Davy et al., 2016), respectively.

rift volcanism during stage-2 (Autin et al., 2010; Nonn et al., 2017; Watremez et al., 2011). This could be shown near $Y = 40$ km along profile L1 and $Y = 31$ km on profile L2 (Figures 3A-1, 3A-2, and 3A-3), where magmatism was substantial and 1-D velocity profiles lie within or below the envelope of Mid-Atlantic Ridge (MAR) igneous crustal values (White et al., 1992). Elevated Vp with a locally increased Vp gradient (>0.5/s) in the intermediate

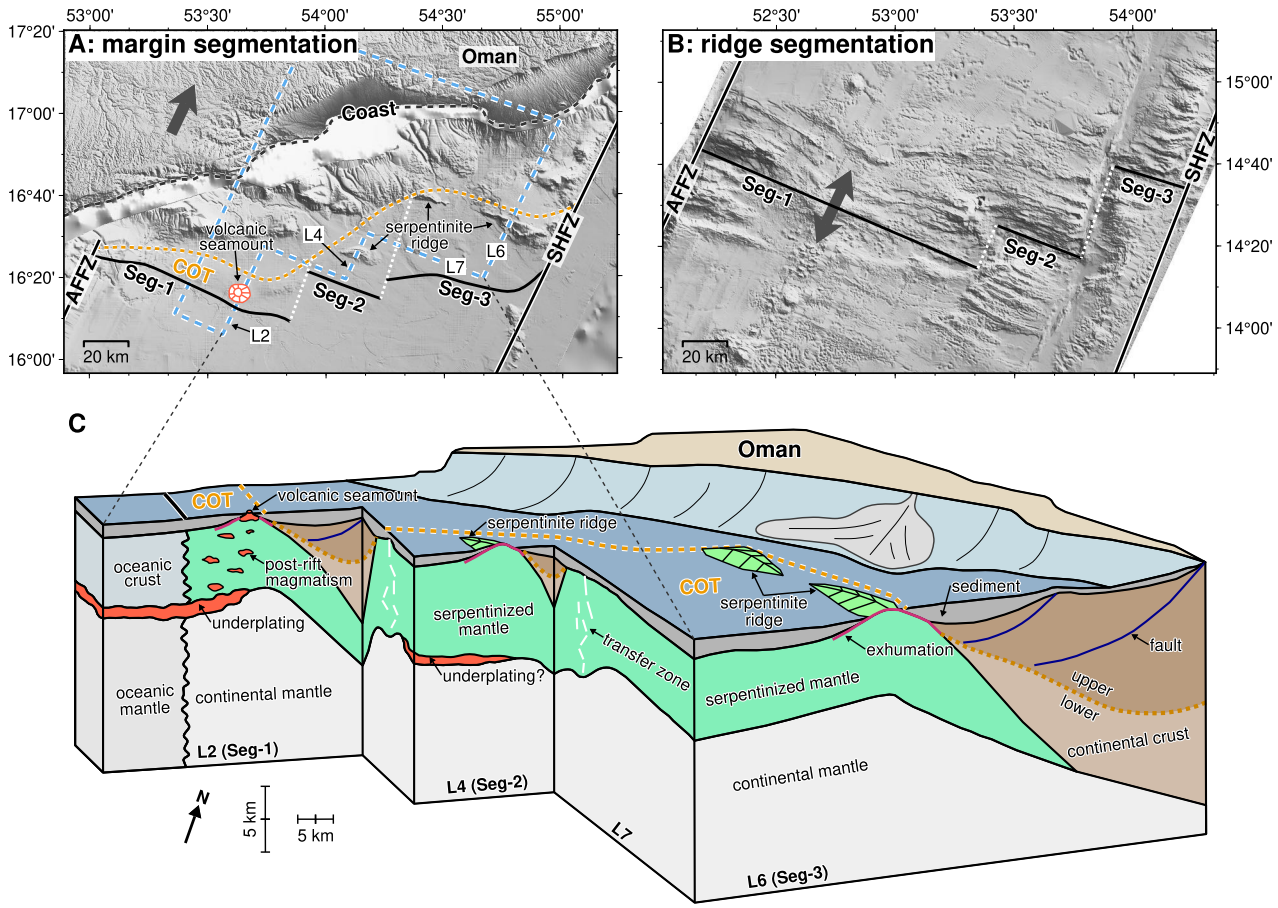

Figure 4. Interpretative sketch for segmentation and modes of continental breakup. (a, b) Segmentation of the rifted margin and the ongoing spreading center, respectively. See locations in Figure 1a. Both depict three segments (black line) separated by two fracture zones (dashed white lines). Blue dashed polygon along profiles L2, L4, L7, and L6 shows the boundary of the 3-D sketch. (c) 3-D schematic diagram showing the modes of continental breakup along and across the COT (VE = 2). Serpentinized mantle is exhumed by detachment faults in all three profiles, with a prevalence that increases eastwardly (i.e., from L2 to L6). Underplating and post-rift magmatism occurred at L2 and possibly at L4.

layer is observed near $Y = 38$ km along profile L2 (Figures 3A-2 and S11B-2 in Supporting Information S1), where 1-D velocity profile (Figure 3A-3) shows similarity to exhumed serpentinized mantle materials, for example, at the ultraslow spreading SWIR 64.5°E (Corbalán et al., 2021; Momoh et al., 2017; Robinson et al., 2024) and the magma-poor West Iberia rifted margin (Davy et al., 2016), and may be subsequently modified by post-rift magmatic intrusions. To the east of profile L2 within the western Seg-1, the crustal thickness rapidly diminishes to 6–8 km toward the ocean (Figure 2b), and the 1-D Vp profiles of this region do not clearly match the envelopes for igneous crust or serpentinized mantle (orange lines in Figure S12B-2 in Supporting Information S1). The source of this post-rift magmatism during stage-2 is not clear, but may be related to the Afar mantle plume and/or small-scale mantle convection (Korostelev et al., 2015; Leroy, d'Acremont et al., 2010; Lucazeau et al., 2008, 2009). Recent studies also suggest that small-scale mantle convection under hyperextended margins may cause a delay in thermal relaxation, potentially triggering post-rift magmatism with elevated heat flow (Pérez-Gussinyé et al., 2024; Zhu & Liu, 2025).

Our 3-D seismic volume, therefore, provides evidence supporting the two-stage COT formation, that is, continental mantle exhumation followed by post-rift magmatism. The base of the crust is defined by the 7.5 km/s isovelocity. Thus, it includes Vp of peridotites with different degrees of serpentinization, igneous rocks, and hybrid peridotite-igneous rocks around intrusion contacts (Figure 4c). Massive magmatic intrusions and associated heat could also reduce the degree of mantle serpentinization through olivine recrystallization and dehydration (Albers et al., 2019; Brindley & Hayami, 1963; Raleigh & Paterson, 1965). The serpentinized mantle near profile L1 is significantly overprinted by robust magmatism, correlated with the reduced crustal velocity (Figure 3A-3). To the

east of profile L2, the residual serpentinized mantle may persist due to limited magmatism. Besides, no serpentinization-related magnetic anomaly is observed at the western Seg-1 (d'Acremont et al., 2006, 2010; Leroy et al., 2004).

2.3. Mantle Exhumation and V-Shaped Continent-Ocean Transition

Mantle exhumation with detachment faulting is typical at magma-poor margins (Minshull, 2009; Pérez-Gussinyé & Reston, 2001; Tucholke et al., 2007), as is the case at the north-eastern Gulf of Aden, evidenced from our 3-D seismic volume. At the central Seg-2 (36 km long) and the eastern Seg-3 (65 km long), where the COT widens from ∼10 to 30–50 km, the seismic crustal thickness ranges between 5 and 8 km mostly with a 1-2 km-thick intermediate layer (Figures 2b and 2e), suggesting very little syn-rift or post-rift magmatism. We observe evidence for serpentinized mantle within these segments, particularly at profiles L3 and L6 (Figures 3B-1 and 3C-2). Velocities increase sharply from 3.5 km/s to 7–8 km/s within 4–5 km below the basement, followed by a lower Vp gradient at greater depths (Figures 3B-3 and 3C-3), which mostly matches serpentinized mantle at the SWIR 64.5°E (Corbalán et al., 2021; Momoh et al., 2017) and the West Iberia margin (Davy et al., 2016), except for the deep part (>4 km below the basement), near $Y = 49$ km of profile L4 (Figures 3B-2 and 3B-3). High Vp gradients (>0.5/s) of the intermediate layer within the COT at profiles L3, L5, and L6 also support this interpretation (Figures S11B-3, S11B-5, and S11B-6 in Supporting Information S1). In addition, linear basement highs, perpendicular to the extension direction, are observed on the seafloor (Figure 4a), spatially linking to the uplifted Vp structures in across-COT profiles L4, L5, and L6 (Figures 3B-2, 3C-1, and 3C-2). Therefore, we interpret these features as serpentinite ridges formed by one or several detachment faults, similar to the West Iberia margin (Davy et al., 2016) and the SWIR 64.5°E (Corbalán et al., 2021; Momoh et al., 2017). These ridges display decreased heat flows, suggesting that they act as recharge zones for hydrothermal circulation (Leroy, Lucazeau, et al., 2010; Lucazeau et al., 2010).

Low-amplitude magnetic anomalies have been observed at the central Seg-2 and the eastern Seg-3 but not at the more volcanic western Seg-1 (Figure 2a), which are locally interpreted as magnetic A6 (20 Ma). These anomalies are likely not an isochron due to the formation of oceanic crust but support peridotite serpentinization (d'Acremont et al., 2006; Leroy et al., 2004; Leroy, Lucazeau, et al., 2010), due to detachment faulting or continuous fault back-rotation (Liu et al., 2022). However, few S reflectors of detachment faults are observed in the multichannel reflection data (Autin et al., 2010; Leroy, Lucazeau, et al., 2010). Assuming that the velocity at depth correlates with the degree of mantle rock serpentinization (Christensen, 2004), our study area shows heterogeneous serpentinization along the strike (Figures 3b and 3c, S12B-2, and S12B-3 in Supporting Information S1). For example, vertical slices across the eastern transfer zone that offsets Seg-2 and Seg-3, show an uplift of Vp and a high Vp gradient (>0.5/s) near $X = 101$ km of profile L7 (Figures 3D-1 and S11B-7 in Supporting Information S1) and $X = 95$ km of profile L8 (Figures 3D-2 and S11B-8 in Supporting Information S1), which is likely associated with serpentinized mantle, due to fluid circulation within the fractured crust and mantle. A relatively high degree of serpentinization likely occurred at $X = 95$ km of profile L8, with a notably low Vp at shallow depths (Figure 3D-3). We interpret this as the arising due to increased cracking during COT-perpendicular shearing, which occurred during the period when the eastern transfer zone was accommodating the obliquity, leading to more extensive hydrothermal circulation and thus a higher degree of serpentinization at shallow depths.

Low Vp is observed at depths >4 km below the serpentinite ridge near $Y = 38$ km of profile L4 (the center of Seg-2), and the seismic crustal thickness is locally up to >8 km and extends into the oceanic crustal domain (Figure 2b), which coincides with a ∼4-km-thick intermediate velocity layer (Figure 2e). This may be attributed to a small amount of magmatic underplating during the COT formation (Figure 4c), due to along-strike melt focusing to the center of the segment, a phenomenon widely observed at slow and ultraslow spreading ridges (Cannat et al., 1999; Lin et al., 1990). Such magmatic underplating is not observed at Seg-3, where the crustal thickness is nearly uniform at 5–6 km (Figure 2b), and its 1-D Vp profiles mostly match serpentinized mantle (Figure 3C-3 and S12B-2 in Supporting Information S1).

The amount of magma supply of the COT, therefore, decreases from the western Seg-1 to the eastern Seg-3, corresponding to an increasing prevalence of serpentinized mantle exhumed by detachment faults (Figure 4c). More detachment faults may accommodate more tectonic strain asymmetrically in the Arabian plate, eventually resulting in a higher time-averaged extension rate and the V-shaped COT (Leroy, Lucazeau, et al., 2010).

Alternatively, the V-shaped configuration of the COT may relate to a westward propagation of the rifting system, similar to the West Iberia margin (Murillas et al., 1990; Pérez-Gussinyé et al., 2003; Péron-Pinvidic & Manatschal, 2009), although no evidence has been found regarding the timing of different propagating phases, such as the graben deepening (Figure 1c) or the sediment thickening (Figure S3B in Supporting Information S1) in the westward direction.

3. Conclusion

Our 3-D seismic velocity model at the north-eastern Gulf of Aden reveals the spatial complexity in crustal evolution of a magma-poor margin during continental breakup. The 45°oblique crustal thinning, coupled with the integration of transfer zones, generates the initial margin segmentation that persists into the progression of seafloor spreading. Our data also display high lateral heterogeneity in crustal features along the Continent-Ocean Transition (COT). Specifically, the narrow COT with thick crusts at the western Seg-1 is influenced by post-rift magmatism emplacing onto exhumed mantle. At the central Seg-2 and eastern Seg-3, where the crusts are relatively thin, mantle exhumation increases eastwardly, interpreted as an eastward increase in time-averaged extension rate due to detachment faulting. This may be ultimately responsible for the formation of the V-shaped COT. We propose that rifted margins naturally exhibit significant along-strike variability in response to different modes and stages of continental breakup, including syn- and post-rift processes, as well as possible pre-rift mantle fertility/hydration (Lizarralde et al., 2007).

Data Availability Statement

Raw seismic data of this study are available (Leroy, 2006). First-arrival picks and the final 3-D Vp model are available (Chen et al., 2024).

Acknowledgments
This manuscript benefited from constructive reviews by Marta Pérez-Gussinyé and Harm Van Avendonk. This work was supported by the ANR YOCMAL project (ANR-07-BLAN-0135). Jie Chen was funded by Naturalia & Biologia and Sorbonne Université. This is IPGP contribution #4283.

References

Albers, E., Schroeder, T., & Bach, W. (2019). Melt impregnation of mantle peridotite facilitates high-temperature hydration and mechanical weakening: Implications for oceanic detachment faults. *Geochemistry, Geophysics, Geosystems*, *20*(1), 84–108. https://doi.org/10.1029/2018GC007783

Autin, J., Leroy, S., Beslier, M. O., d'Acremont, E., Razin, P., Ribodetti, A., et al. (2010). Continental break-up history of a deep magma-poor margin based on seismic reflection data (northeastern Gulf of Aden margin, offshore Oman). *Geophysical Journal International*, *180*(2), 501–519. https://doi.org/10.1111/j.1365-246X.2009.04424.x

Boddupalli, B., Minshull, T. A., Bayrakci, G., Lymer, G., Klaeschen, D., & Reston, T. J. (2022). Insights into exhumation and mantle hydration processes at the deep galicia margin from a 3D high-resolution seismic velocity model. *Journal of Geophysical Research: Solid Earth*, *127*(7). https://doi.org/10.1029/2021JB023220

Brindley, G. W., & Hayami, R. (1963). Kinetics and mechanisms of dehydration and recrystallization of serpentine—I. *Clays and Clay Minerals*, *12*, 35–47. https://doi.org/10.1346/ccmn.1963.0120107

Brune, S., Kolawole, F., Olive, J. A., Stamps, D. S., Buck, W. R., Buiter, S. J. H., et al. (2023). Geodynamics of continental rift initiation and evolution. *Nature Reviews Earth & Environment*, *4*(4), 235–253. https://doi.org/10.1038/s43017-023-00391-3

Cannat, M., Rommevaux-Jestin, C., Sauter, D., Deplus, C., & Mendel, V. (1999). Formation of the axial relief at the very slow spreading Southwest Indian Ridge (49° to 69°E). *Journal of Geophysical Research*, *104*(B10), 22825–22843. https://doi.org/10.1029/1999jb900195

Carlson, R. L., & Miller, D. J. (2004). Influence of pressure and mineralogy on seismic velocities in oceanic gabbros: Implications for the composition and state of the lower oceanic crust. *Journal of Geophysical Research*, *109*(B9), 2003JB002699. https://doi.org/10.1029/2003JB002699

Chen, J., Leroy, S., Watremez, L., & Robinson, A. (2024). Research Data for "Mantle exhumation and post-rift magmatism at an oblique magma-poor continental margin" [Dataset]. *figshare*. https://doi.org/10.6084/M9.FIGSHARE.25751733

Chen, J., Zhang, T., Li, H., Tao, C., Cannat, M., & Sauter, D. (2023). Evolution of enhanced magmatism at the ultraslow spreading Southwest Indian Ridge between 46°E and 53.5°E. *Tectonophysics*, *860*, 229903. https://doi.org/10.1016/j.tecto.2023.229903

Christensen, N. I. (2004). Serpentinites, peridotites, and seismology. *International Geology Review*, *46*(9), 795–816. https://doi.org/10.2747/0020-6814.46.9.795

Corbalán, A., Nedimović, M. R., Louden, K. E., Cannat, M., Grevemeyer, I., Watremez, L., & Leroy, S. (2021). Seismic velocity structure along and across the ultraslow-spreading southwest Indian ridge at 64°30′E showcases flipping detachment faults. *Journal of Geophysical Research: Solid Earth*, *126*(10), e2021JB022177. https://doi.org/10.1029/2021JB022177

d'Acremont, E., Leroy, S., Beslier, M. O., Bellahsen, N., Fournier, M., Robin, C., et al. (2005). Structure and evolution of the eastern Gulf of Aden conjugate margins from seismic reflection data. *Geophysical Journal International*, *160*(3), 869–890. https://doi.org/10.1111/j.1365-246X.2005.02524.x

d'Acremont, E., Leroy, S., Maia, M., Gente, P., & Autin, J. (2010). Volcanism, jump and propagation on the Sheba ridge, eastern Gulf of Aden: Segmentation evolution and implications for oceanic accretion processes. *Geophysical Journal International*, *180*(2), 535–551. https://doi.org/10.1111/j.1365-246X.2009.04448.x

d'Acremont, E., Leroy, S., Maia, M., Patriat, P., Beslier, M. O., Bellahsen, N., et al. (2006). Structure and evolution of the eastern Gulf of Aden: Insights from magnetic and gravity data (Encens-Sheba MD117 cruise). *Geophysical Journal International*, *165*(3), 786–803. https://doi.org/10.1111/j.1365-246X.2006.02950.x

Davy, R. G., Minshull, T. A., Bayrakci, G., Bull, J. M., Klaeschen, D., Papenberg, C., et al. (2016). Continental hyperextension, mantle exhumation, and thin oceanic crust at the continent-ocean transition, West Iberia: New insights from wide-angle seismic. *Journal of Geophysical Research: Solid Earth*, *121*(5), 3177–3199. https://doi.org/10.1002/2016JB012825

Duclaux, G., Huismans, R. S., & May, D. A. (2020). Rotation, narrowing, and preferential reactivation of brittle structures during oblique rifting. *Earth and Planetary Science Letters*, *531*, 115952. https://doi.org/10.1016/j.epsl.2019.115952

Dunn, R. A., Lekić, V., Detrick, R. S., & Toomey, D. R. (2005). Three-dimensional seismic structure of the mid-Atlantic Ridge (35°N): Evidence for focused melt supply and lower crustal dike injection. *Journal of Geophysical Research*, *110*(9), 1–17. https://doi.org/10.1029/2004JB003473

Fournier, M., Bellahsen, N., Fabbri, O., & Gunnell, Y. (2004). Oblique rifting and segmentation of the NE Gulf of Aden passive margin. *Geochemistry, Geophysics, Geosystems*, *5*(11). https://doi.org/10.1029/2004GC000731

Geoffroy, L. (2005). Volcanic passive margins. *Comptes Rendus Geoscience*, *337*(16), 1395–1408. https://doi.org/10.1016/j.crte.2005.10.006

Korostelev, F., Leroy, S., Keir, D., Ahmed, A., Boschi, L., Rolandone, F., et al. (2015). Upper mantle structure of the southern Arabian margin: Insights from teleseismic tomography. *Geosphere*, *11*(5), 1262–1278. https://doi.org/10.1130/GES01159.1

Lavier, L. L., & Manatschal, G. (2006). A mechanism to thin the continental lithosphere at magma-poor margins. *Nature*, *440*(7082), 324–328. https://doi.org/10.1038/nature04608

Leroy, S. (2006). ENCENS cruise, RV L'Atalante [Dataset]. https://doi.org/10.17600/6010030

Leroy, S., d'Acremont, E., Tiberi, C., Basuyau, C., Autin, J., Lucazeau, F., & Sloan, H. (2010). Recent off-axis volcanism in the eastern Gulf of Aden: Implications for plume-ridge interaction. *Earth and Planetary Science Letters*, *293*(1–2), 140–153. https://doi.org/10.1016/j.epsl.2010.02.036

Leroy, S., Gente, P., Fournier, M., d'Acremont, E., Patriat, P., Beslier, M. O., et al. (2004). From rifting to spreading in the eastern gulf of aden: A geophysical survey of a young oceanic basin from margin to margin. *Terra Nova*, *16*(4), 185–192. https://doi.org/10.1111/j.1365-3121.2004.00550.x

Leroy, S., Lucazeau, F., d'Acremont, E., Watremez, L., Autin, J., Rouzo, S., et al. (2010). Contrasted styles of rifting in the eastern gulf of aden: A combined wide-angle, multichannel seismic, and heat flow survey. *Geochemistry, Geophysics, Geosystems*, *11*(7). https://doi.org/10.1029/2009GC002963

Leroy, S., Razin, P., Autin, J., Bache, F., d'Acremont, E., Watremez, L., et al. (2012). From rifting to oceanic spreading in the gulf of aden: A synthesis. *Arabian Journal of Geosciences*, *5*(5), 859–901. https://doi.org/10.1007/s12517-011-0475-4

Lin, J., Purdy, G. M., Schouten, H., Sempere, J.-C., & Zervas, C. (1990). Evidence from gravity data for focused magmatic accretion along the Mid-Atlantic Ridge. *Nature*, *344*(6267), 627–632. https://doi.org/10.1038/344627a0

Liu, Z., Pérez-Gussinyé, M., Rüpke, L., Muldashev, I. A., Minshull, T. A., & Bayrakci, G. (2022). Lateral coexistence of ductile and brittle deformation shapes magma-poor distal margins: An example from the West Iberia-Newfoundland margins. *Earth and Planetary Science Letters*, *578*, 117288. https://doi.org/10.1016/j.epsl.2021.117288

Lizarralde, D., Axen, G. J., Brown, H. E., Fletcher, J. M., González-Fernández, A., Harding, A. J., et al. (2007). Variation in styles of rifting in the Gulf of California. *Nature*, *448*(7152), 466–469. https://doi.org/10.1038/nature06035

Lucazeau, F., Leroy, S., Autin, J., Bonneville, A., Goutorbe, B., Watremez, L., et al. (2009). Post-rift volcanism and high heat-flow at the ocean-continent transition of the eastern Gulf of Aden. *Terra Nova*, *21*(4), 285–292. https://doi.org/10.1111/j.1365-3121.2009.00883.x

Lucazeau, F., Leroy, S., Bonneville, A., Goutorbe, B., Rolandone, F., d'Acremont, E., et al. (2008). Persistent thermal activity at the eastern gulf of Aden after continental break-up. *Nature Geoscience*, *1*(12), 854–858. https://doi.org/10.1038/ngeo359

Lucazeau, F., Leroy, S., Rolandone, F., d'Acremont, E., Watremez, L., Bonneville, A., et al. (2010). Heat-flow and hydrothermal circulation at the ocean-continent transition of the eastern gulf of Aden. *Earth and Planetary Science Letters*, *295*(3–4), 554–570. https://doi.org/10.1016/j.epsl.2010.04.039

Minshull, T. A. (2009). Geophysical characterisation of the ocean-continent transition at magma-poor rifted margins. *Comptes Rendus Geoscience*, *341*(5), 382–393. https://doi.org/10.1016/j.crte.2008.09.003

Momoh, E., Cannat, M., Watremez, L., Leroy, S., & Singh, S. C. (2017). Quasi-3-D seismic reflection imaging and wide-angle velocity structure of nearly amagmatic oceanic lithosphere at the ultraslow-spreading southwest Indian ridge. *Journal of Geophysical Research: Solid Earth*, *122*(12), 9511–9533. https://doi.org/10.1002/2017JB014754

Murillas, J., Mougenot, D., Boulot, G., Comas, M. C., Banda, E., & Mauffret, A. (1990). Structure and evolution of the galicia interior basin (Atlantic western Iberian continental margin). *Tectonophysics*, *184*(3–4), 297–319. https://doi.org/10.1016/0040-1951(90)90445-E

Nonn, C., Leroy, S., Khanbari, K., & Ahmed, A. (2017). Tectono-sedimentary evolution of the eastern Gulf of Aden conjugate passive margins: Narrowness and asymmetry in oblique rifting context. *Tectonophysics*, *721*, 322–348. https://doi.org/10.1016/j.tecto.2017.09.024

Nonn, C., Leroy, S., Lescanne, M., & Castilla, R. (2019). Central Gulf of Aden conjugate margins (Yemen-Somalia): Tectono-sedimentary and magmatism evolution in hybrid-type margins. *Marine and Petroleum Geology*, *105*, 100–123. https://doi.org/10.1016/j.marpetgeo.2018.11.053

Pallister, J. S., McCausland, W. A., Jónsson, S., Lu, Z., Zahran, H. M., El Hadidy, S., et al. (2010). Broad accommodation of rift-related extension recorded by dyke intrusion in Saudi Arabia. *Nature Geoscience*, *3*(10), 705–712. https://doi.org/10.1038/ngeo966

Pérez-Gussinyé, M., Ranero, C. R., Reston, T. J., & Sawyer, D. (2003). Mechanisms of extension at nonvolcanic margins: Evidence from the Galicia interior basin, west of Iberia. *Journal of Geophysical Research*, *108*(B5), 2001JB000901. https://doi.org/10.1029/2001JB000901

Pérez-Gussinyé, M., & Reston, T. J. (2001). Rheological evolution during extension at nonvolcanic rifted margins: Onset of serpentinization and development of detachments leading to continental breakup. *Journal of Geophysical Research*, *106*(B3), 3961–3975. https://doi.org/10.1029/2000JB900325

Pérez-Gussinyé, M., Xin, Y., Cunha, T., Ram, R., Andrés-Martínez, M., Dong, D., & García-Pintado, J. (2024). Synrift and post-rift thermal evolution of rifted margins: A re-evaluation of classic models of extension. *Geological Society, London, Special Publications*, *547*(1), 13–38. https://doi.org/10.1144/SP547-2023-128

Péron-Pinvidic, G., & Manatschal, G. (2009). The final rifting evolution at deep magma-poor passive margins from Iberia-Newfoundland: A new point of view. *International Journal of Earth Sciences*, *98*(7), 1581–1597. https://doi.org/10.1007/s00531-008-0337-9

Raleigh, C. B., & Paterson, M. S. (1965). Experimental deformation of serpentinite and its tectonic implications. *Journal of Geophysical Research*, *70*(16), 3965–3985. https://doi.org/10.1029/jz070i016p03965

Robinson, A., Watremez, L., Leroy, S., Minshull, T., Cannat, M., & Corbalán, A. (2024). A 3-D seismic tomographic study of spreading structures and smooth seafloor generated by detachment faulting–the ultra-slow spreading southwest Indian ridge at 64° 30'E. In *EGU general assembly 2024*.

Sauter, D., Manatschal, G., Kusznir, N., Masquelet, C., Werner, P., Ulrich, M., et al. (2023). Ignition of the southern Atlantic seafloor spreading machine without hot-mantle booster. *Scientific Reports*, *13*(1), 1195. https://doi.org/10.1038/s41598-023-28364-y

Sauter, D., Patriat, P., Rommevaux-Jestin, C., Cannat, M., & Briais, A. (2001). The Southwest Indian Ridge between 49° 15′E and 57°E: Focused accretion and magma redistribution. *Earth and Planetary Science Letters*, *192*(3), 303–317. https://doi.org/10.1016/S0012-821X(01)00455-1

Tard, F., Masse, P., Walgenwitz, F., & Gruneisen, P. (1991). The volcanic passive margin in the vicinity of Aden, Yemen. *Bulletin - Centres de Recherche Exploration-Production Elf-Aquitaine*, *15*(1), 1–9.

Tiberi, C., Leroy, S., d'Acremont, E., Bellahsen, N., Ebinger, C., Al-lazki, A., & Pointu, A. (2007). Crustal geometry of the northeastern Gulf of Aden passive margin: Localization of the deformation inferred from receiver function analysis. *Geophysical Journal International*, *168*(3), 1247–1260. https://doi.org/10.1111/j.1365-246X.2006.03294.x

Tucholke, B. E., Sawyer, D. S., & Sibuet, J. C. (2007). Breakup of the Newfoundland-Iberia rift. *Geological Society - Special Publications*, *282*(1), 9–46. https://doi.org/10.1144/SP282.2

Van Avendonk, H. J. A., Holbrook, W. S., Nunes, G. T., Shillington, D. J., Tucholke, B. E., Louden, K. E., et al. (2006). Seismic velocity structure of the rifted margin of the eastern Grand Banks of Newfoundland, Canada. *Journal of Geophysical Research*, *111*(B11), 2005JB004156. https://doi.org/10.1029/2005JB004156

Watremez, L., Leroy, S., Rouzo, S., d'Acremont, E., Unternehr, P., Ebinger, C., et al. (2011). The crustal structure of the north-eastern Gulf of Aden continental margin: Insights from wide-angle seismic data. *Geophysical Journal International*, *184*(2), 575–594. https://doi.org/10.1111/j.1365-246X.2010.04881.x

White, R. S., McKenzie, D., & O'Nions, R. K. (1992). Oceanic crustal thickness from seismic measurements and rare earth element inversions. *Journal of Geophysical Research*, *97*(B13), 19683–19715. https://doi.org/10.1029/92jb01749

White, R. S., & Smith, L. K. (2009). Crustal structure of the Hatton and the conjugate east Greenland rifted volcanic continental margins, NE Atlantic. *Journal of Geophysical Research*, *114*(2). https://doi.org/10.1029/2008JB005856

White, R. S., Smith, L. K., Roberts, A. W., Christie, P. A. F., Kusznir, N. J., Roberts, A. M., et al. (2008). Lower-crustal intrusion on the North Atlantic continental margin. *Nature*, *452*(7186), 460–464. https://doi.org/10.1038/nature06687

Winterer, E. L., & Bosellini, A. (1981). Subsidence and sedimentation on Jurassic passive continental margin, southern Alps, Italy. *American Association of Petroleum Geologists Bulletin*, *65*(3), 394–421. https://doi.org/10.1306/2f9197e2-16ce-11d7-8645000102c1865d

Zelt, C. A., & Barton, P. J. (1998). Three-dimensional seismic refraction tomography: A comparison of two methods applied to data from the Faeroe basin. *Journal of Geophysical Research*, *103*(B4), 7187–7210. https://doi.org/10.1029/97JB03536

Zhang, J., Zhao, M., Ding, W., Ranero, C. R., Sallares, V., Gao, J., et al. (2023). New insights into the rift-to-drift process of the northern south China sea margin constrained by a three-dimensional wide-angle seismic velocity model. *Journal of Geophysical Research: Solid Earth*, *128*(4). https://doi.org/10.1029/2022JB026171

Zhu, W., & Liu, S. (2025). Heat flow and thermal structure of the South China Sea. *Earth-Science Reviews*, *261*, 105028. https://doi.org/10.1016/j.earscirev.2024.105028

References From the Supporting Information

Korenaga, J., Holbrook, W. S., Kent, G. M., Kelemen, P. B., Detrick, R. S., Larsen, H. C., et al. (2000). Crustal structure of the southeast Greenland margin from joint refraction and reflection seismic tomography. *Journal of Geophysical Research: Solid Earth*, *105*(B9), 21591–21614.

Watremez, L., Helen Lau, K. W., Nedimovic, M. R., & Louden, K. E. (2015). Traveltime tomography of a dense wide-angle profile across Orphan Basin. *Geophysics*, *80*(3), B69–B82. https://doi.org/10.1190/geo2014-0377.1

Weatherall, P., Marks, K. M., Jakobsson, M., Schmitt, T., Tani, S., Arndt, J. E., et al. (2015). A new digital bathymetric model of the world's oceans. *Earth and Space Science*, *2*(8), 331–345. https://doi.org/10.1002/2015EA000107

Zelt, C. A. (1998). Lateral velocity resolution from three-dimensional seismic refraction data. *Geophysical Journal International*, *135*(3), 1101–1112. https://doi.org/10.1046/j.1365-246X.1998.00695.x

Zhang, J., & Toksöz, M. N. (1998). Nonlinear refraction traveltime tomography. *Geophysics*, *63*(5), 1726–1737. https://doi.org/10.1190/1.1444468

Supporting Information for

Mantle exhumation and post-rift magmatism at an oblique magma-poor continental margin

Jie Chen[1,2,3], Sylvie Leroy[2], Louise Watremez[4], Adam H. Robinson[5]

[1] Université Paris Cité, Institut de physique du globe de Paris, 75005 Paris, France

[2] Sorbonne Université, CNRS-INSU, Institut des Sciences de la Terre Paris, 75005, Paris, France

[3] Laboratoire de Géologie, Ecole Normale Supérieure, PSL Research University, Paris 75005, France

[4] Université de Lille, CNRS, Université Littoral Côte d'Opale, IRD, UMR 8187, Laboratoire d'Océanologie et de Géosciences, Lille, France

[5] School of Ocean and Earth Science, University of Southampton, Southampton, UK

Corresponding author: Jie Chen (chen@geologie.ens.fr)

This PDF file includes:

- Text S1
- Fig. S1-S15
- Table S1-S3
- References

Text S1

Data acquisition

The 3-D wide-angle seismic refraction data used in this paper were collected by a combined onshore-offshore survey during the Encens cruise in 2006 (Leroy, 2006; Leroy et al., 2010; Watremez et al., 2011), and comprise ~7500 offshore air-gun shots along 15 track lines (1110 km in total) with a shot interval of ~150 m (60 s at a speed of ~5 knots). The source is made up of an array of 18 air guns with a total volume of 138 L, towed at 22–25 m depth. The data were recorded by 35 ocean-bottom seismometers (OBS) deployed at intervals of 10-15 km and 13 land seismometers (Fig. 1C). The internal clocks of the OBSs were synchronized with a linear drift correction during deployment and recovery, and the OBS positions were relocated to their true position on the seafloor by the inversion of the direct wave arrival times (Watremez et al., 2011).

Traveltime Picking

P-wave first arrival traveltimes are picked from the vertical component and the hydrophone of the receivers (e.g., Fig. S1; note that land stations only have the vertical component). Approximately 180 000 first arrivals are picked within shot-receiver offsets up to 140 km for OBSs and 190 km for land seismometers (Fig. S2A). To account for errors of picking and instrument location, uncertainties are artificially assigned to traveltime picks based on the shot-receiver offset, which are 20, 50, 80, 100, and 150 ms for offsets at 0-5, 5-10, 10-20, 20-50, and >50 km, respectively (Table S1).

Setup for seismic tomography in FAST

Travel times were inverted in 3-D using the FAST (First-Arrival Seismic Tomography), which applies a regularized inversion method to iteratively construct a smooth 3-D velocity model (Zelt & Barton, 1998). The parameters used in the inversions are summarized in Table S2 (Zelt & Barton, 1998). Each starting model is inverted with 10 iterations and 6 values of the trade-off parameter (λ). The model space has dimensions of 215 × 155 × 37 km in X (-5 to 210 km), Y (-5 to 150 km), and Z (-2 to 35 km below sea level). The node spacing is 0.5 km both laterally and vertically for the forward grid, and 1 km laterally and 0.5 km vertically for the inverse grid. In the oceanic domain, the seafloor is constructed from the shipboard bathymetry data, and the sediment thickness is constructed using multichannel seismic reflection data (Autin et al., 2010; d'Acremont et al., 2005). The land topography is constructed using the GEBCO database (Weatherall et al., 2015).

Starting 3-D velocity model

The starting 3-D P-wave velocity (Vp) model is composed of separate velocity profiles

for the oceanic and terrestrial domains (Fig. S3), with a straight boundary to represent the simplified COT, here referred to as continent-ocean boundary (COB). An example is shown in Fig. S3. In the oceanic domain, the Vp is fixed in the water layer at 1.5 km/s, and linearly increases from 1.6 to 4 km/s in the sediment layer and from 4 to 7.5 km/s from the basement top to the Moho (Fig. S3F). The Moho (defined as 7.5 km/s) is located at 6 km (i.e., crustal thickness) below the basement top. For the terrestrial domain, (north to the coast in Fig. S3a), the starting model linearly increases from 4 km/s at the surface to 7.5 km/s at the Moho (Fig. S3e). The upper mantle has a thickness of 3 km with Vp linearly increasing from 7.5 to 8 km/s. Vp at the base of the model is 8.2 km/s. The COB location is inferred from previous 2-D seismic tomography (Leroy et al., 2010; Watremez et al., 2011), corresponding to a velocity gradient towards the terrestrial domain with ΔY (90 km) and ΔZ (15 km) (e.g., Fig. S3D).

Monte-Carlo analysis

We apply a Monte-Carlo analysis (Korenaga et al., 2000), in order to determine the uncertainty on calculated velocities and to test any issues which may relate to final model dependence on the choice of starting model. A set of 100 starting velocity models are created by perturbing each starting model parameter within the ranges given in Table S3. In addition, we add random noise to the picked first arrival traveltimes (Watremez et al., 2015; Zhang & Toksöz, 1998), linking to 1) instrumental uncertainties with the maximum value of ±62.5 ms and 2) picking uncertainties with a Gaussian distribution scaled according to the assigned uncertainties, which yields a set of 100 synthetic traveltime data sets.

100 random combinations of starting velocity models and synthetic traveltimes are inverted as above, with the final model of each inversion chosen as the iteration when $\chi^2 \approx 1$. The 100 final models are averaged, and the velocity standard deviation is calculated (Fig. S7). Traveltime residuals of the final model do not show any significant dependence on receivers or shot-receiver offsets (Fig. S2), with only slightly higher residuals at land stations.

Checkerboard test and model resolution

To assess the spatial resolution of the final velocity model, we perform a set of checkerboard tests (Fig. S13-S14), following the previous approach (Zelt, 1998). An alternating polarity, cubic checkerboard pattern with velocity perturbation ±5% is applied to the final velocity model. Synthetic traveltimes are calculated by forward ray tracing using the shot-receiver geometries, and random noise is added proportionately to the instrumental and picking uncertainties. These resulting travel times are then re-inverted to recover the

checkerboard pattern. 9 different checkerboard cell sizes are tested, from 4 to 20 km at 2 km intervals (Fig. S14). Each cell size has 8 different patterns with spatially shifting of 0, 0.5, 1, and 1.5 of the cell size in all three directions, as well as horizontally rotating of 0° and 45° (e.g., Fig. S13A-S13H for the checkerboard of the cell size at 10 km) in order to reduce potential effects of preferential ray-path or checkerboard null-plane alignments. Resolvability is represented as the semblance, calculated using an operator radius the same as the checkerboard cell size. Semblance is averaged across lateral shifts and rotations for each checkerboard size (Fig. S14). A semblance of ≥0.7 is considered as well resolved (Zelt, 1998). For lower cell sizes and shallower depths, the semblance is higher and thus the lateral resolution is also higher (Fig. S14). The model surrounding the COT exhibits a good spatial resolution at Z≤12 km with a cell size of 10 km (Fig. S14).

We combine all areas of semblance of 0.7 for 9 different cell sizes and interpolate them to generate a map of spatial resolution (Fig. S8 and S11). The higher ray density at the central and shallow part of the model enables a better resolution, while the deep part and the edge of the model have the lowest spatial resolution due to the lack of ray coverage (Fig. S6 and S8).

Comparing with previous 2-D Vp tomography

We compare our results of the 3-D Vp tomography model with previous co-incident 2-D Vp tomography models (Fig. S15) (Leroy et al., 2010; Watremez et al., 2011). 8 velocity profiles (L1-L5 and L7-L9) were constructed in 2-D using Ranvir, which includes both first arrivals, and reflections from the top of the oceanic basement and the Moho (PmP) (Watremez et al., 2011). This modelling approach includes sharp interfaces at the e.g., oceanic basement and the Moho, which cannot be modelled using the FAST inversion approach. The location of the Moho in the 2-D profiles is comparable to the 7.5 km/s iso-velocity contour in our 3-D model, especially at the COT and the oceanic crust (e.g., L2 in Fig. S15A-2 and L5 in Fig. S15C-1), suggesting that this velocity in our model represents a good proxy of the Moho location. The difference between the Moho in the 2-D and the 7.5 km/s iso-velocity in 3-D is larger in the continental domain (e.g., L2 in Fig. S15A-2, L3 in Fig. S15B-1, L8 in Fig. S15D-2, and L9 in Fig. S15D-3), probably due to the lack of the rays in both models. The crustal thickness in the continental domain of our model is not considered as well defined. Besides, both 2-D and the 3-D models have a good agreement in imaging small-scale Vp features in the shallow region (<5 km below the seafloor), e.g., the spur-shaped basement structure at X=52 km of profile L4 (Fig. S15B-2) and seamounts at X=31 km of profile L2 (Fig. S15A-2).

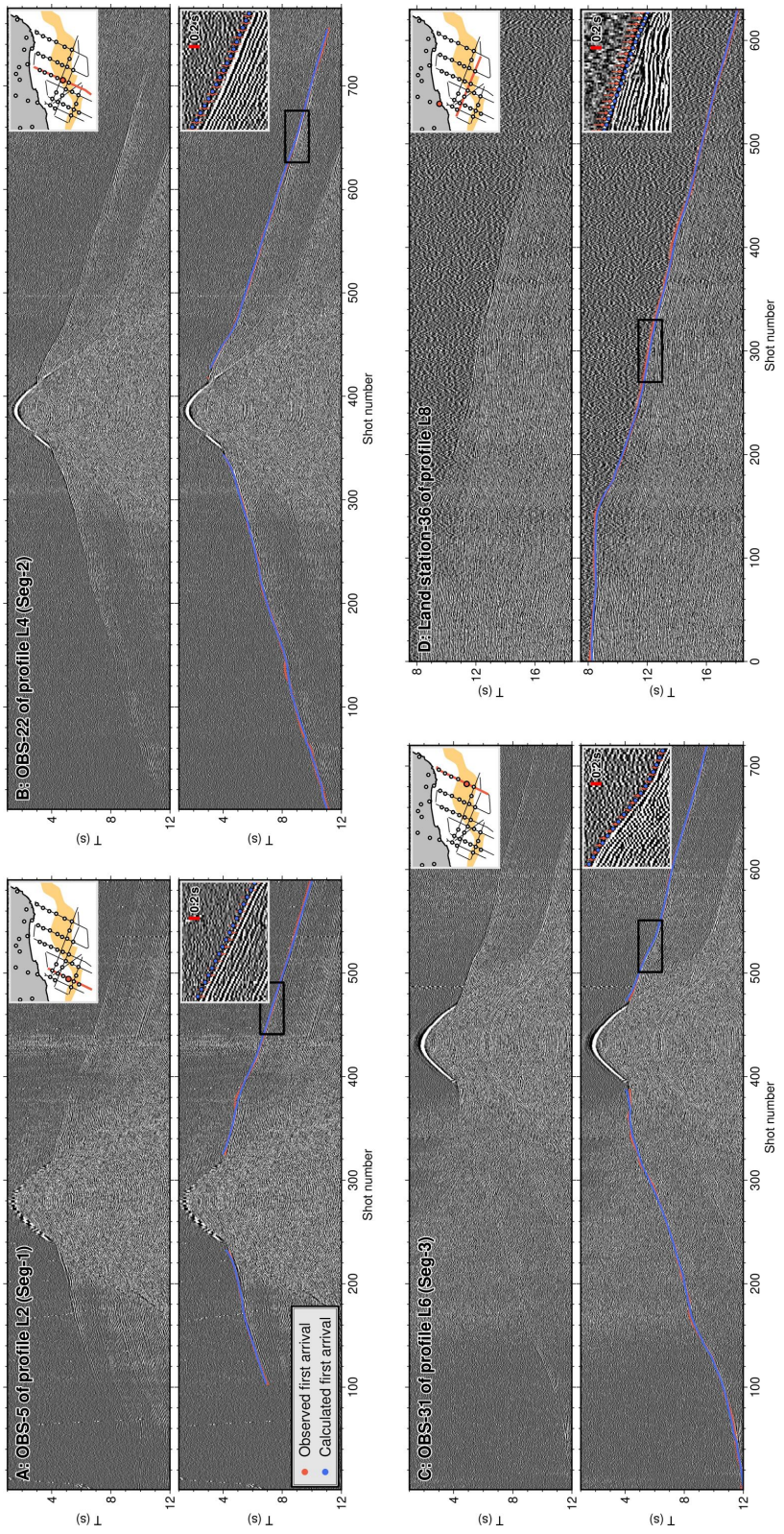

Figure S 1. **Examples of seismic records.** No reduction or filter is applied. Upper panels: uninterpreted seismic records. The inset maps show the location of the shot track (red line) and OBS or land station (red circle). Lower panels: interpreted seismic records with observed (red dots with uncertainties) and calculated (blue dots) first arrivals. The inset is the close-up within the black rectangle. Red bar is the time scale of 0.2 s.

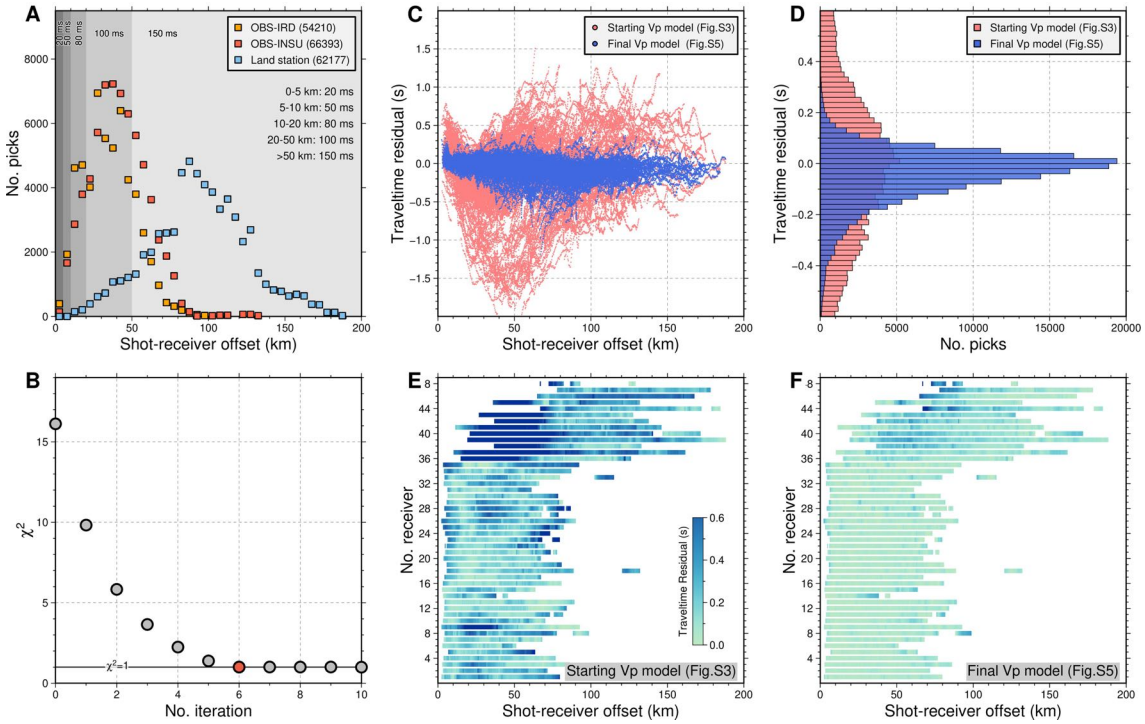

Figure S 2. **3-D model travel-time fit analysis.** (**A**) First-arrival picking number recorded by OBSs and land stations. Shot-receiver offset dependent picking uncertainties are indicated. (B) Reduction of the χ^2 with respect to the number of iterations in FAST, using the starting Vp model in Fig. S3. The inverted Vp model with $\chi^2 \approx 1$ at end of iteration 6 (red circle) is chosen for the final model. (C) and (D) Traveltime residuals of the starting Vp model in Fig. S3 (pink) and the final Vp model (blue, average of 100 Monte-Carlo final models). (E) and (F) Traveltime residuals for each receiver binned at 0.5 km source-receiver offset intervals for the starting Vp model in Fig. S3 and the final Vp model, respectively.

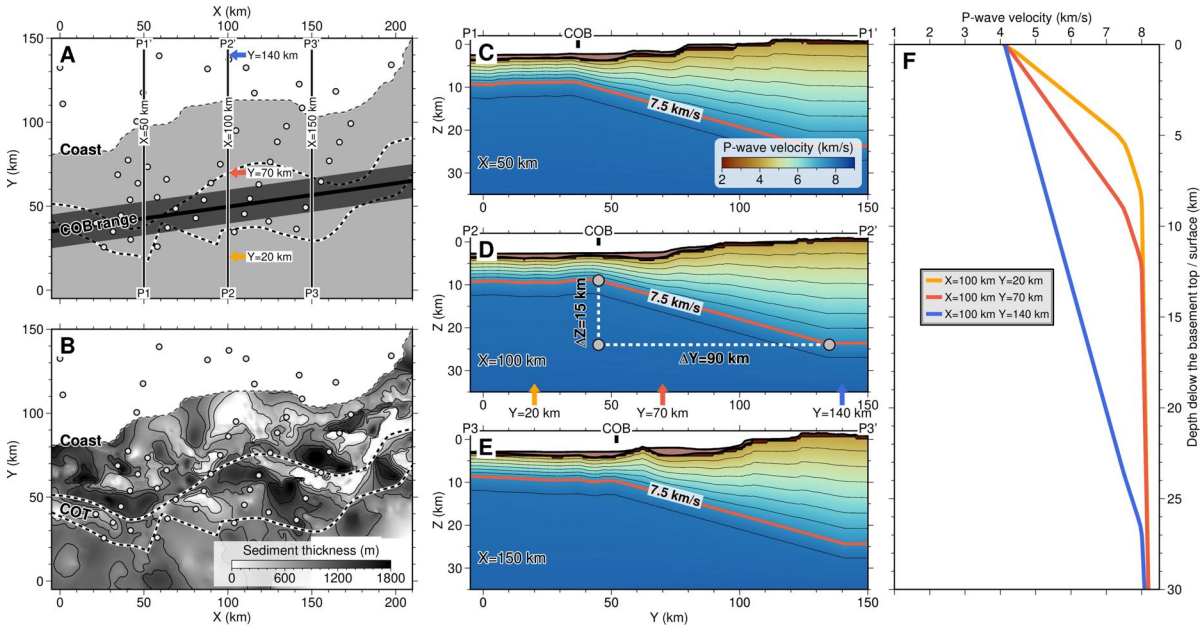

Figure S 3. **Central case of starting Vp models, with parameters in the middle of the ranges of the Monte-Carlo analysis.** (**A**) Simplified structural map showing the coast, the COT (dashed contour), and a simplified continent-ocean boundary (COB) and its range (shaded area). (**B**) Map of sediment thickness (Autin et al., 2010; d'Acremont et al., 2005). (**C**) - (**E**) Vertical Vp slices through the central case of starting Vp models along profiles P1-P1', P2-P2', and P3-P3'. The COB used in this starting model is shown as the black solid line in Fig. S3A. The contour interval is 0.5 km/s. The slope of the 7.5 km/s iso-velocity, to the north of the COB, is defined by ΔY (90 km) and ΔZ (15 km) based on previous 2-D seismic tomography (Leroy et al., 2010; Watremez et al., 2011). (**F**) Three 1-D Vp profiles of the P2-P2' profile represent the oceanic crust (orange line), the COT crust (red line), and the continental crust (blue line).

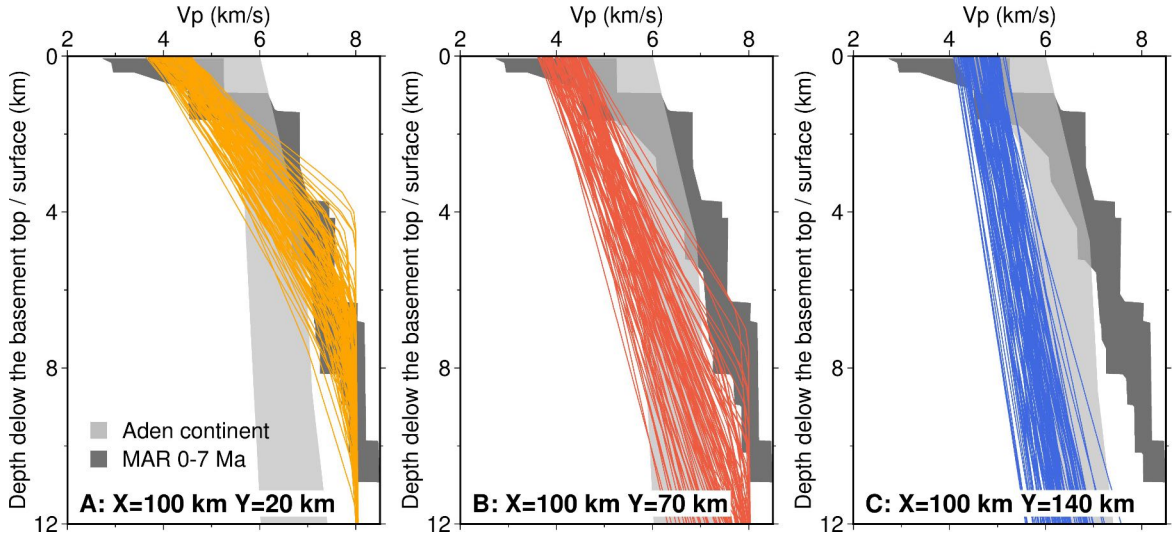

Figure S 4. **1-D Vp starting models, extracted from 100 random 3-D starting Vp models in Monte-Carlo analysis.** (**A**), (**B**), and (**C**) represent oceanic, COT, and continental crusts, respectively; their locations are shown as arrows with the same color in the P2-P2' profile of Fig. S3A. Velocity envelopes in black and gray represent the oceanic crust of the Mid-Atlantic Ridge (MAR) (White et al., 1992) and the continental crust of the north-eastern Gulf of Aden (Leroy et al., 2010; Watremez et al., 2011), respectively.

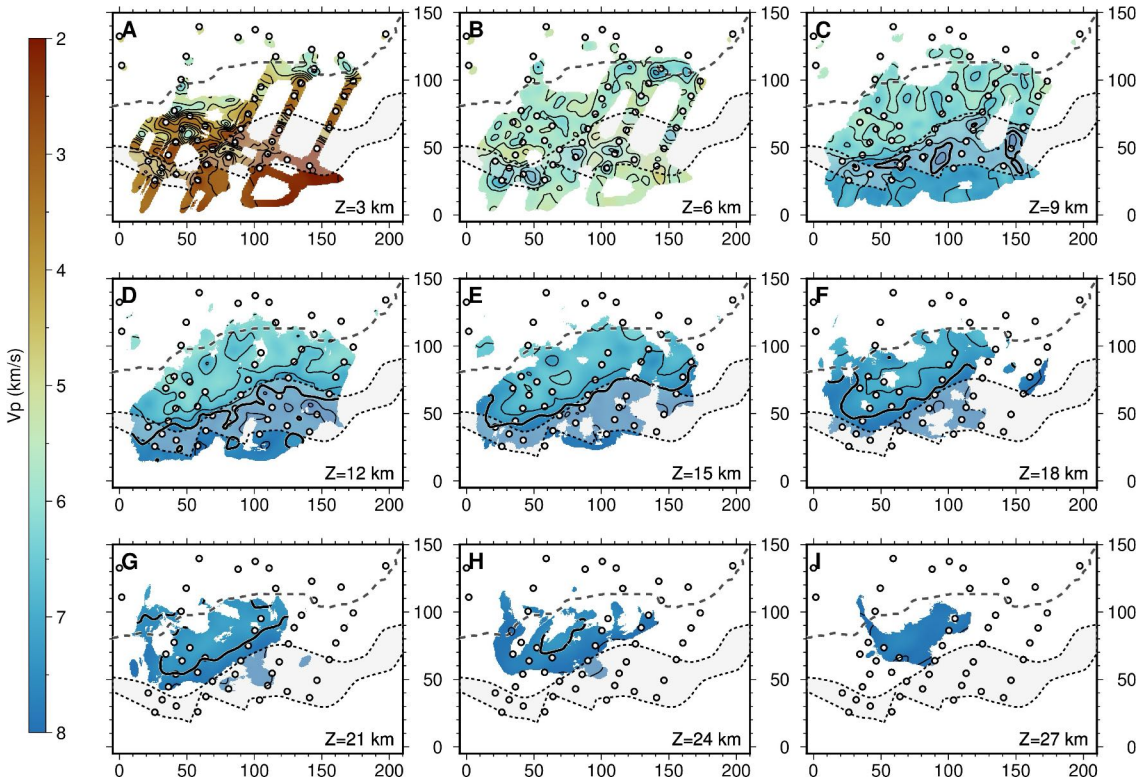

Figure S 5. **Depth slices (below the sea level) through the final Vp model.** White masks correspond to areas without ray coverage. Contour interval is 0.5 km/s, highlighting the 7.5 km/s. Coast and COT are plotted as dashed line and gray shaded area, respectively.

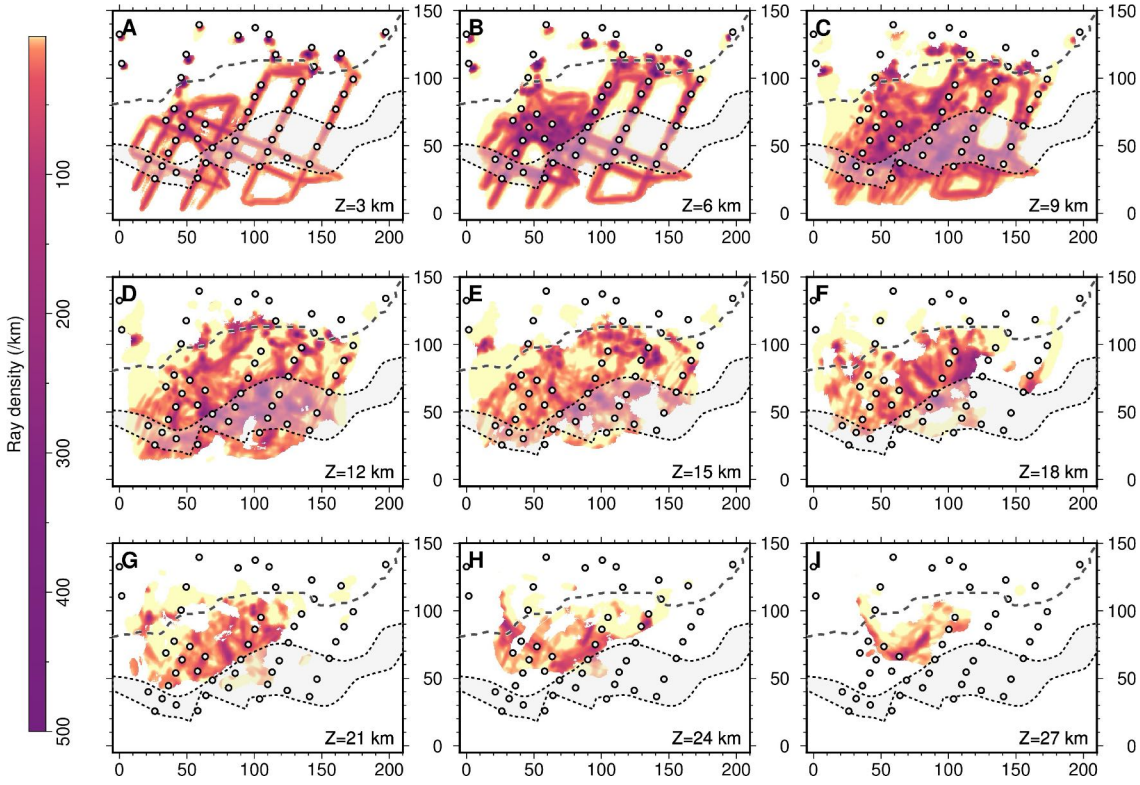

Figure S 6. **Depth slices of ray density through the final Vp model.** Symbols are identical to Fig. S5.

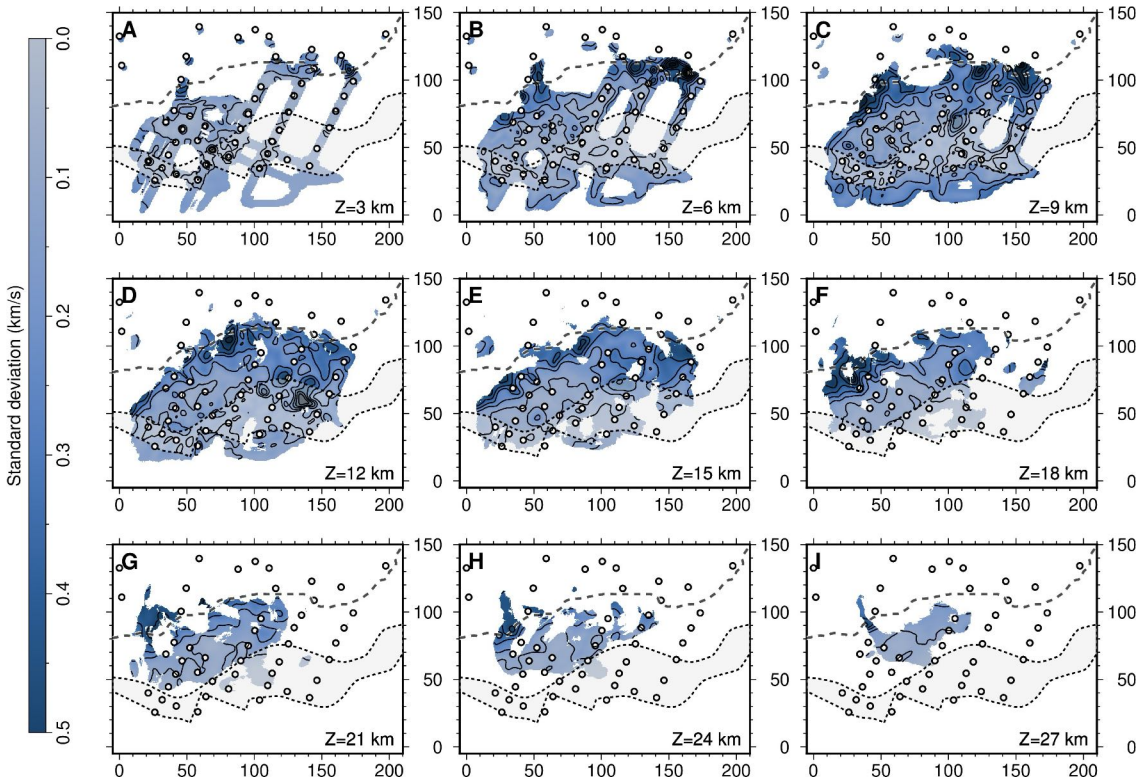

Figure S 7. **Depth slices of standard deviation of 100 Monte-Carlo final Vp models.** The contour interval is 0.1 km/s. Symbols are identical to Fig. S5.

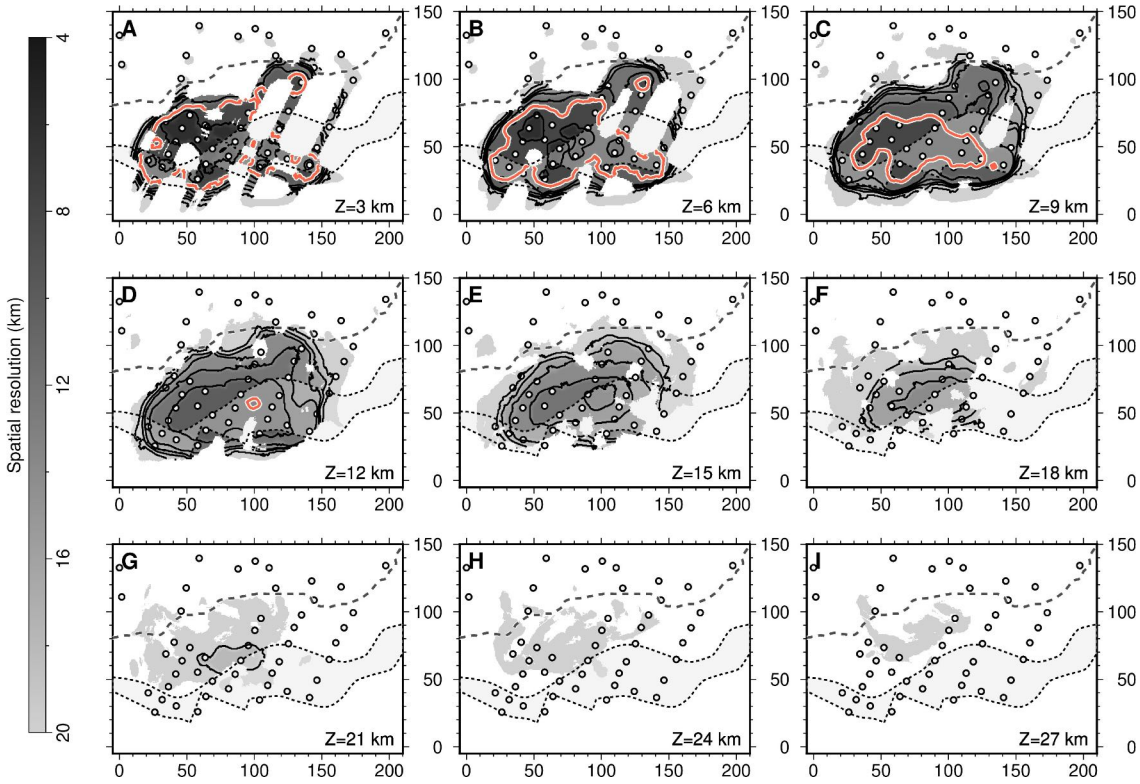

Figure S 8. **Depth slices of spatial resolution, based on the minimum cell size in checkerboard test with semblance>0.7**. Contour interval is 2 km, highlighting the 10 km (in red). Symbols are identical to Fig. S5.

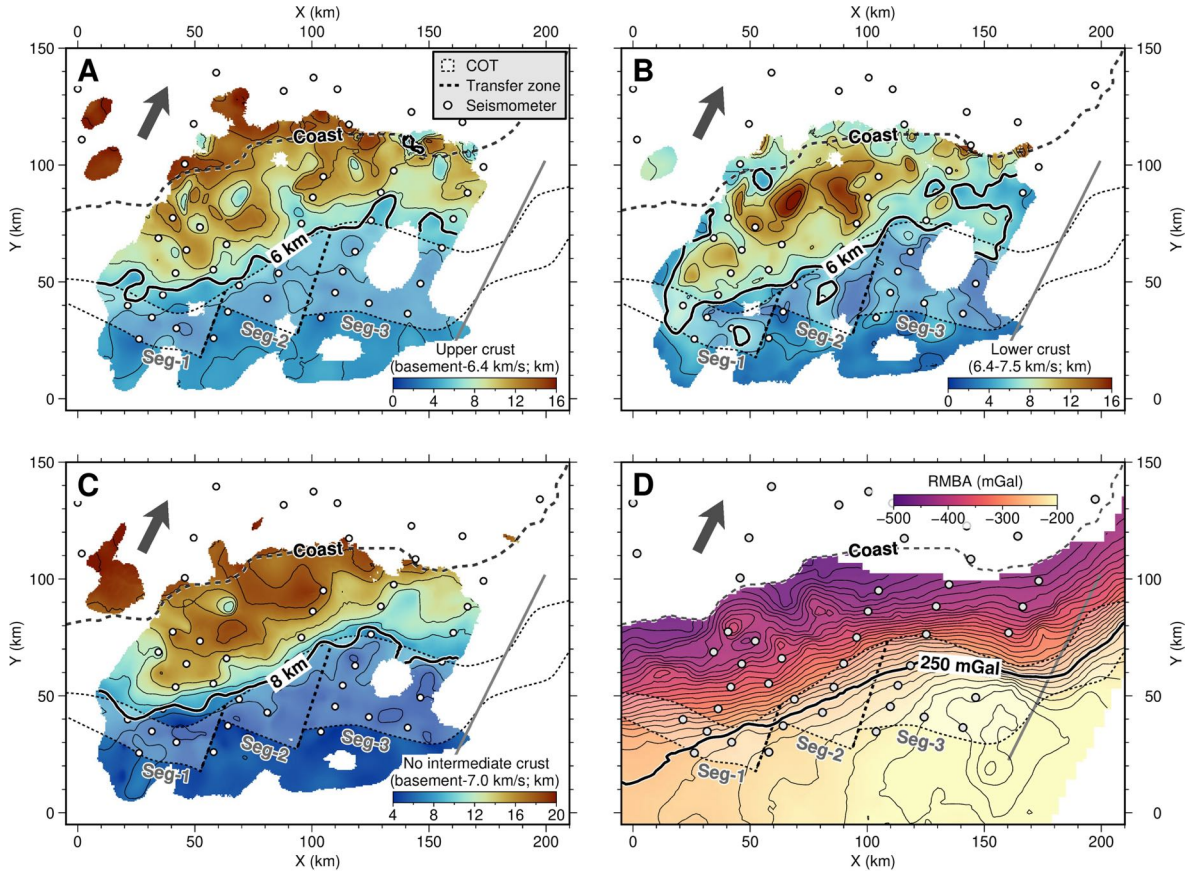

Figure S 9. **Map view of the final Vp model and RMBA.** White masks correspond to areas without ray coverage. Gray arrows show the extension direction. (**A**) Upper crustal thickness, calculated between the basement top and the 6.4 km/s iso-velocity. Contour interval is 2 km, highlighting the 6 km. (**B**) Lower crustal thickness, calculated between the 6.4 and the 7.5 km/s iso-velocities. Contour interval is 2 km, highlighting the 6 km. (**C**) Crustal thickness without the intermediate velocity, calculated between the basement top and the 7.5 km/s iso-velocity. Contour interval is 2 km, highlighting the 8 km. (**D**) Residual mantle bouguer gravity anomaly (RMBA) (d'Acremont et al., 2010). Contour interval is 10 mGal, highlighting the 250 mGal.

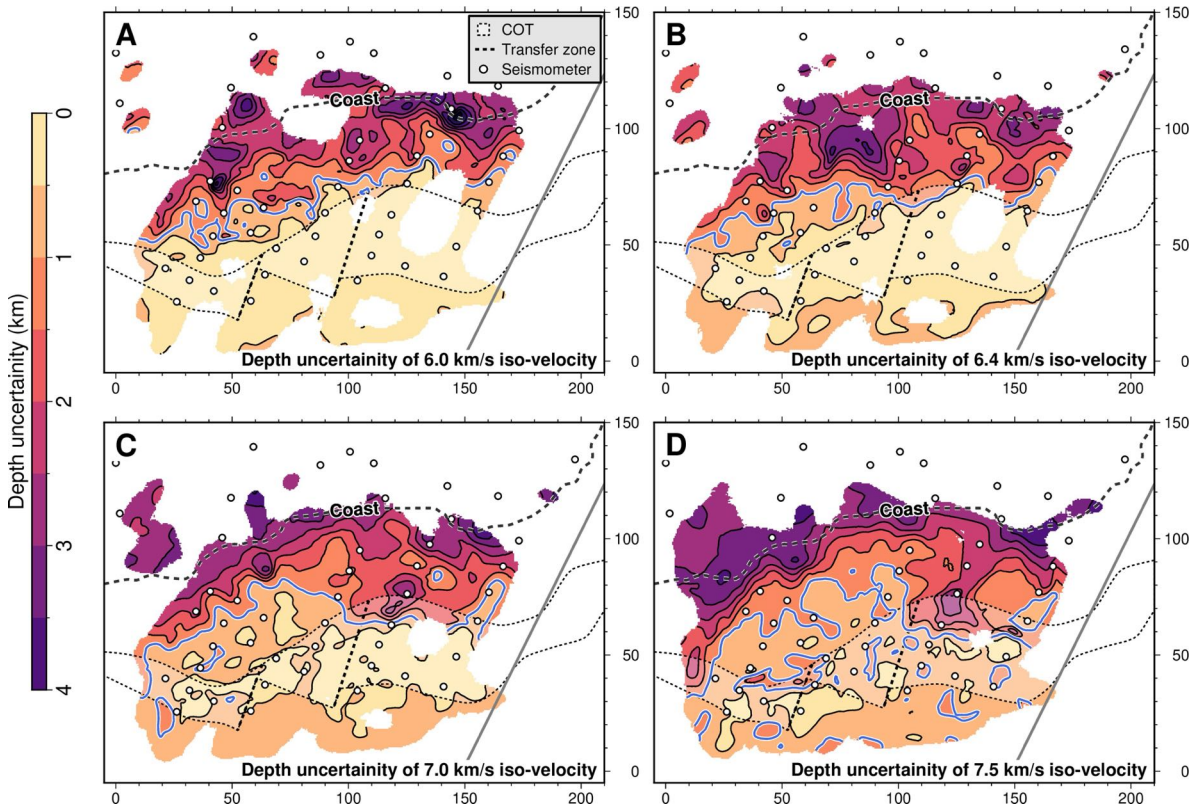

Figure S 10. **Map view of depth uncertainties of iso-velocities at 6.0 km/s (A), 6.4 km/s (B), 7.0 km/s (C), and 7.5 km/s (D)**, derived from the standard deviation of 100 Monte-Carlo final Vp models. White masks correspond to areas without ray coverage. Contour interval is 0.5 km, highlighting the 1 km (in blue).

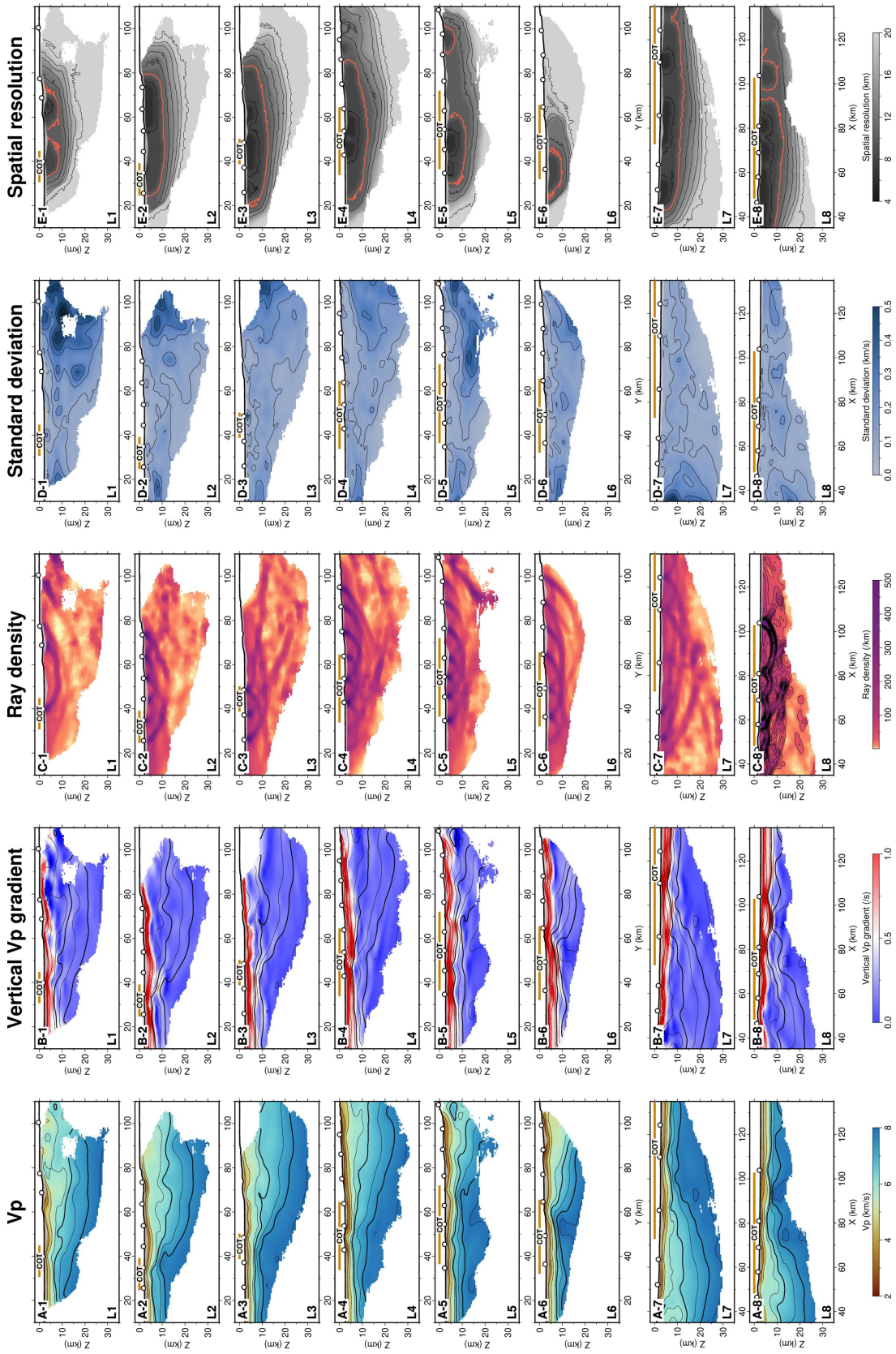

Figure S 11. **Vertical slices of Vp (A), vertical Vp gradient (B), ray density (C), standard deviation of 100 Monte-Carlo final Vp models (D), and spatial resolution (E).** Locations of 8 profiles (L1-L8) are shown in Fig. 2A.

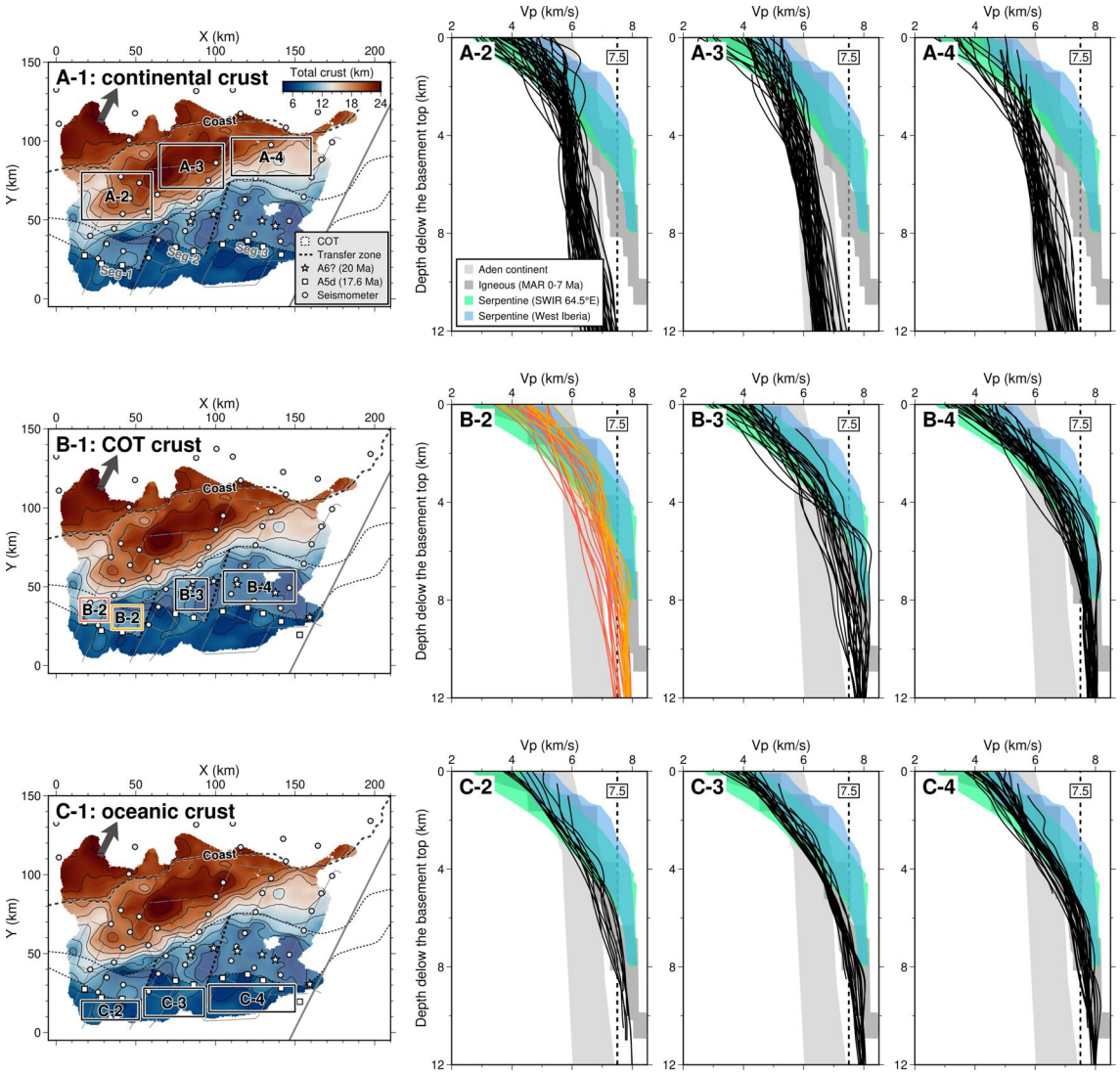

Figure S 12. **1-D Vp profiles of continental (A), COT (B), and oceanic (C) crusts.** 1-D profiles are sampled with an interval of 5 km in both X and Y directions, within the corresponding boxes in A-1, B-1, and C-1 that are crustal thickness map in Fig. 2B. Velocity envelopes in light and dark gray represent the continental crust of the north-eastern Gulf of Aden (Leroy et al., 2010; Watremez et al., 2011) and the igneous crust of the MAR 0-7 Ma (White et al., 1992), respectively. Green and blue envelopes represent serpentinized mantle of the ultraslow spreading SWIR 64.5°E (Corbalán et al., 2021; Momoh et al., 2017) and the magma-poor West Iberia rifted margin (Davy et al., 2016), respectively. Note that red and orange boxes in B-1 show the locations of corresponding colored 1-D profiles in B-2.

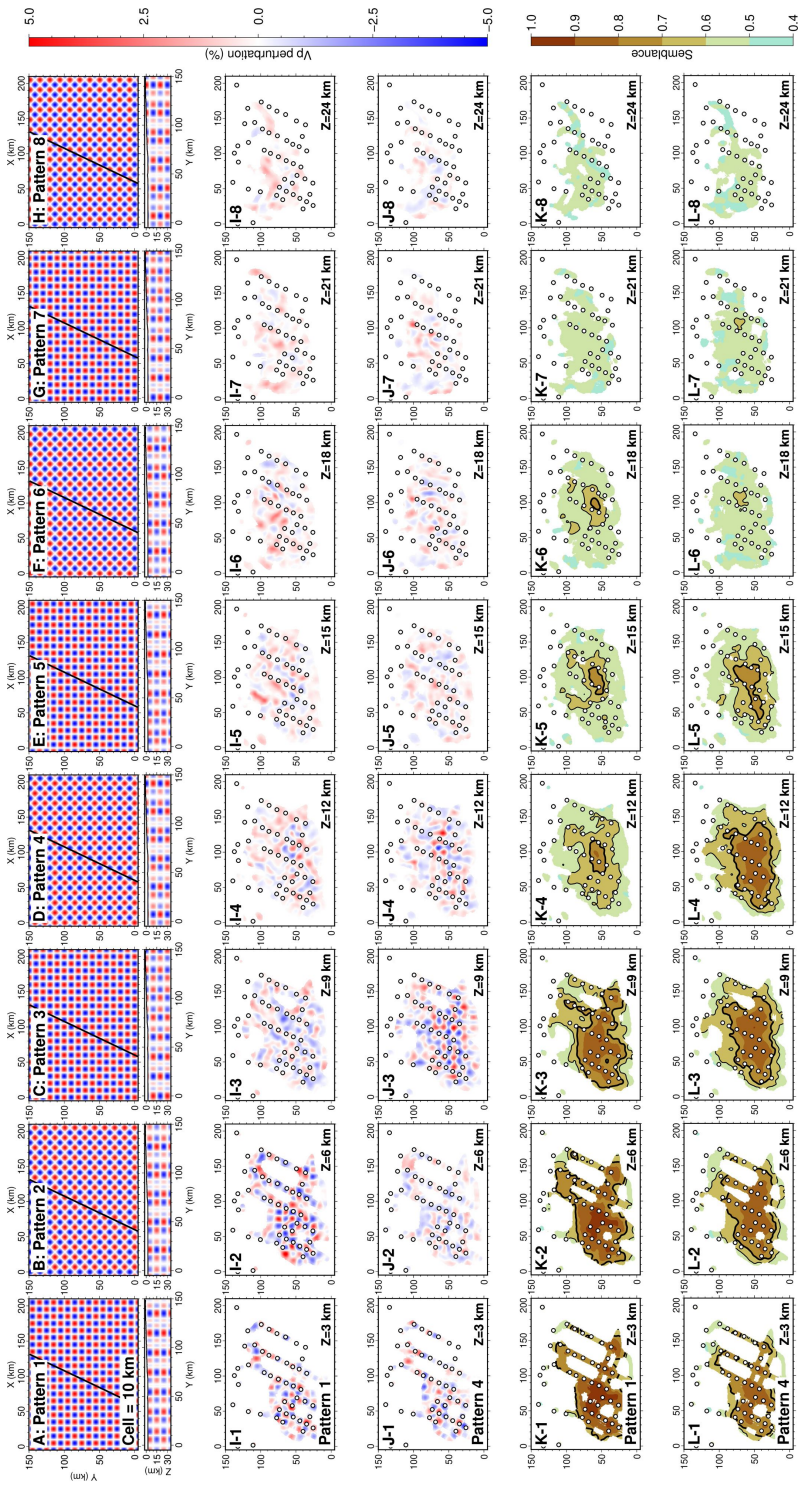

Figure S 13. **Checkerboard tests with cell size of 10 km.** (**A**) - (**H**) 8 different input pattens with shifting of 0, 0.5, 1, and 1.5 of the cell size in X, Y, and Z directions, and rotations of 0° and 45°. Lower panels show vertical slices along black line in upper panels. (**I**) and (**K**) Semblance of Pattern 1 at different depths, with no shifting or rotation of the input pattern. Contours of the semblance of 0.6 (thin line) and 0.7 (thick line) are plotted. (**J**) and (**L**) Semblance of Pattern 4, with shifts of 0.5 of the cell size and 45° rotation applied to input pattern.

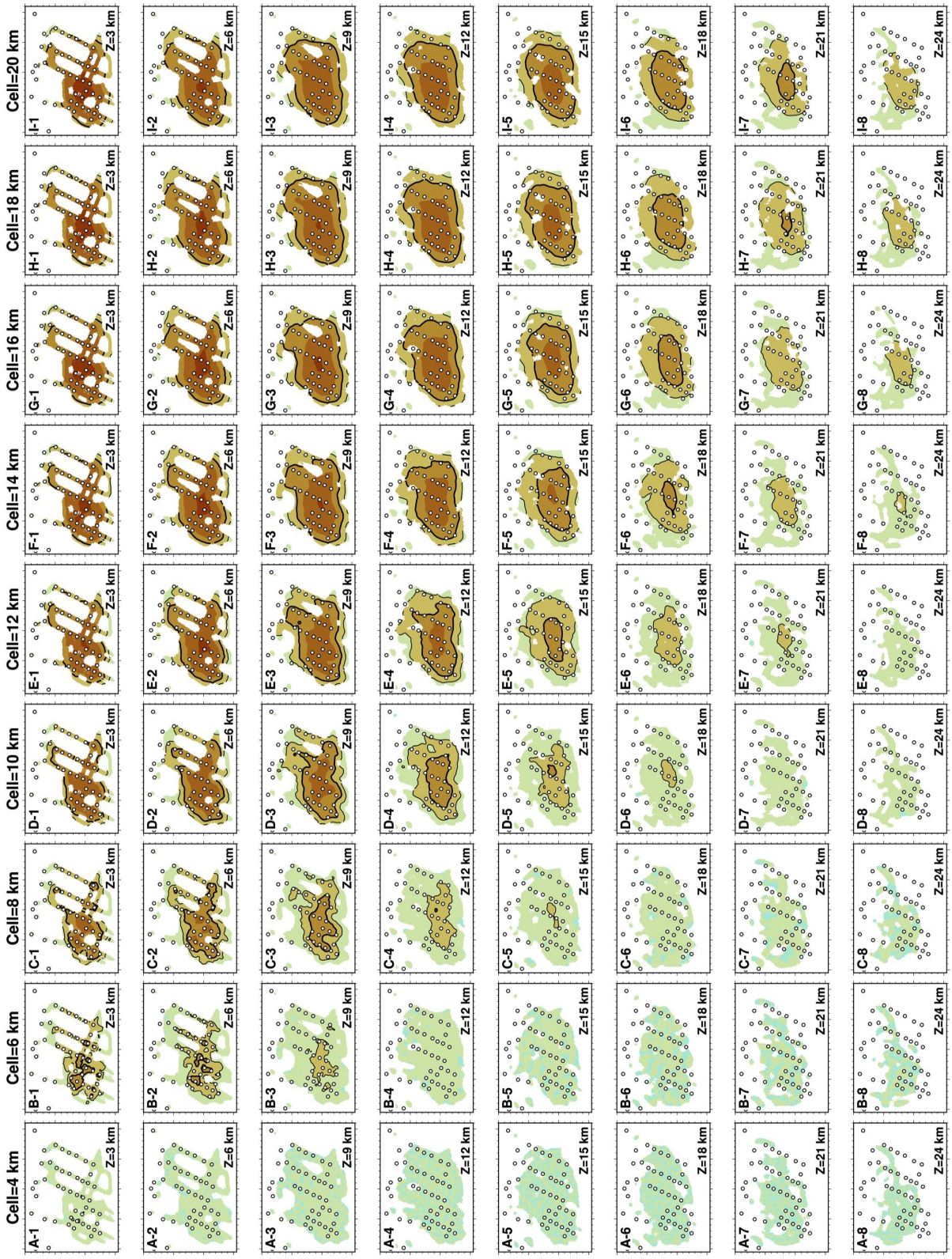

Figure S 14. **Averaged semblance of 8 checkerboard patterns for cell sizes of 4 to 20 km.** Contours of the semblance of 0.6 (thin line) and 0.7 (thick line) are plotted.

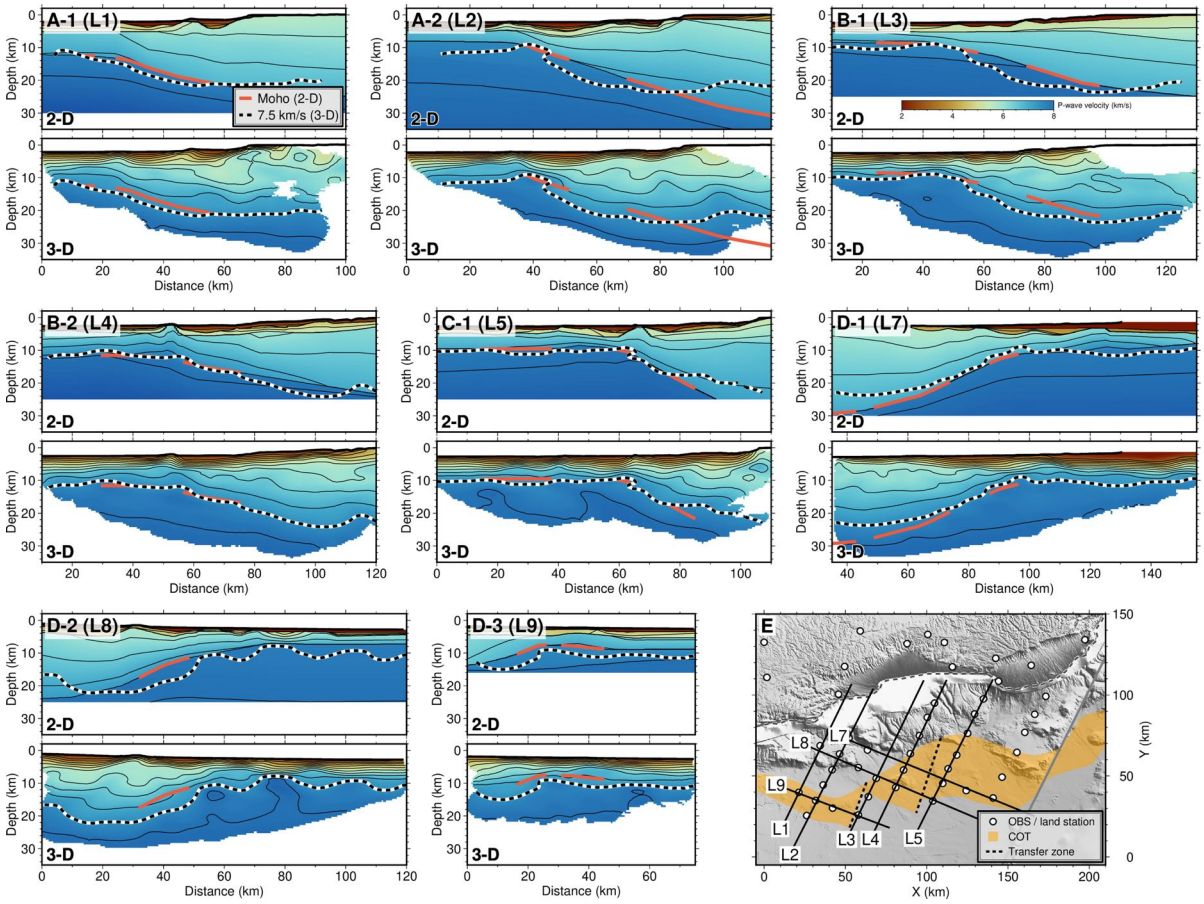

Figure S 15. **Comparison of previous 2-D (upper panels) and 3-D (lower panels) Vp models.** Red lines are Moho interfaces built with PmP reflections by 2-D Vp models using Ranvir algorithm (Leroy et al., 2010; Watremez et al., 2011). Contour interval is 0.5 km/s. Dashed lines are 7.5 km/s iso-velocities from our 3-D Vp models.

Range of shot-receiver offset (km)	Assigned uncertainty to traveltime picks (ms)
0-5	20
5-10	50
10-20	80
20-50	100
>50	150

Table S 1. **Assigned uncertainty for the FAST inversion model.**

Inversion parameter	Value
No. iteration	10
Lambda (λ)	6
Lambda0 (λ0)	100
Lambda reduction factor	1.414
Alpha (α)	0.95
Smoothness factor (sz)	0.125
Model dimensions - X×Y×Z	215×155×74 km
Forward spacing - horizontal	0.5 km
Forward spacing - vertical	0.5 km
Inversion spacing - horizontal	1 km
Inversion spacing - vertical	0.5 km

Table S 2. **Summary of inversion parameters for the FAST inversion model.**

Parameter	Minimum	Maximum	Example (Fig. S3)	unit
Velocity at the continental surface	3.5	4.5	4	km/s
Velocity at the seafloor	1.5	2	1.6	km/s
Velocity at the basement top	3.5	4.5	4	km/s
Velocity of the mantle	7.0	8.0	7.5	km/s
Thickness of the oceanic crust	4.0	8.0	6	km
Thickness of the upper mantle	1.5	4.5	3	km
∆Y	50	100	90	km
∆Z	5	20	15	km
Shift of continent-ocean boundary	-10 (south)	10 (north)	0	km

Table S 3. **Parameters of the starting model used in the Monte-Carlo analysis.**

References

Autin, J., Leroy, S., Beslier, M. O., d'Acremont, E., Razin, P., Ribodetti, A., et al. (2010). Continental break-up history of a deep magma-poor margin based on seismic reflection data (northeastern Gulf of Aden margin, offshore Oman). *Geophysical Journal International*, *180*(2), 501–519. https://doi.org/10.1111/j.1365-246X.2009.04424.x

Corbalán, A., Nedimović, M. R., Louden, K. E., Cannat, M., Grevemeyer, I., Watremez, L., & Leroy, S. (2021). Seismic Velocity Structure Along and Across the Ultraslow-Spreading Southwest Indian Ridge at 64°30′E Showcases Flipping Detachment Faults. *Journal of Geophysical Research: Solid Earth*, *126*(10), e2021JB022177. https://doi.org/10.1029/2021JB022177

d'Acremont, E., Leroy, S., Beslier, M. O., Bellahsen, N., Fournier, M., Robin, C., et al. (2005). Structure and evolution of the eastern Gulf of Aden conjugate margins from seismic reflection data. *Geophysical Journal International*, *160*(3), 869–890. https://doi.org/10.1111/j.1365-246X.2005.02524.x

d'Acremont, E., Leroy, S., Maia, M., Gente, P., & Autin, J. (2010). Volcanism, jump and propagation on the Sheba ridge, eastern Gulf of Aden: Segmentation evolution and implications for oceanic accretion processes. *Geophysical Journal International*, *180*(2), 535–551. https://doi.org/10.1111/j.1365-246X.2009.04448.x

Davy, R. G., Minshull, T. A., Bayrakci, G., Bull, J. M., Klaeschen, D., Papenberg, C., et al. (2016). Continental hyperextension, mantle exhumation, and thin oceanic crust at the continent-ocean transition, West Iberia: New insights from wide-angle seismic. *Journal of Geophysical Research: Solid Earth*, *121*(5), 3177–3199. https://doi.org/10.1002/2016JB012825

Korenaga, J., Holbrook, W. S., Kent, G. M., Kelemen, P. B., Detrick, R. S., Larsen, H. C., et al. (2000). Crustal structure of the southeast Greenland margin from joint refraction and reflection seismic tomography. *Journal of Geophysical Research: Solid Earth*, *105*(B9), 21591–21614. https://doi.org/10.1029/2000jb900188

Leroy, S. (2006). ENCENS cruise, RV L'Atalante. https://doi.org/10.17600/6010030

Leroy, S., Lucazeau, F., d'Acremont, E., Watremez, L., Autin, J., Rouzo, S., et al. (2010). Contrasted styles of rifting in the eastern Gulf of Aden: A combined wide-angle, multichannel seismic, and heat flow survey. *Geochemistry, Geophysics, Geosystems*, *11*(7), n/a-n/a. https://doi.org/10.1029/2009GC002963

Momoh, E., Cannat, M., Watremez, L., Leroy, S., & Singh, S. C. (2017). Quasi-3-D Seismic Reflection Imaging and Wide-Angle Velocity Structure of Nearly Amagmatic Oceanic Lithosphere at the Ultraslow-Spreading Southwest Indian Ridge. *Journal of Geophysical Research: Solid Earth*, *122*(12), 9511–9533. https://doi.org/10.1002/2017JB014754

Watremez, L., Leroy, S., Rouzo, S., d'Acremont, E., Unternehr, P., Ebinger, C., et al. (2011). The crustal structure of the north-eastern Gulf of Aden continental margin: Insights from wide-angle seismic data. *Geophysical Journal International*, *184*(2), 575–594. https://doi.org/10.1111/j.1365-246X.2010.04881.x

Watremez, L., Helen Lau, K. W., Nedimovic, M. R., & Louden, K. E. (2015). Traveltime tomography of a dense wide-angle profile across Orphan Basin. *Geophysics*, *80*(3), B69–B82. https://doi.org/10.1190/geo2014-0377.1

Weatherall, P., Marks, K. M., Jakobsson, M., Schmitt, T., Tani, S., Arndt, J. E., et al. (2015). A new digital bathymetric model of the world's oceans. *Earth and Space Science*, *2*(8), 331–345. https://doi.org/10.1002/2015EA000107

White, R. S., McKenzie, D., & O'Nions, R. K. (1992). Oceanic crustal thickness from seismic measurements and rare earth element inversions. *Journal of Geophysical Research*, *97*(B13). https://doi.org/10.1029/92jb01749

Zelt, C. A. (1998). Lateral velocity resolution from three-dimensional seismic refraction data. *Geophysical Journal International*, *135*(3), 1101–1112. https://doi.org/10.1046/j.1365-246X.1998.00695.x

Zelt, C. A., & Barton, P. J. (1998). Three-dimensional seismic refraction tomography: A comparison of two methods applied to data from the Faeroe Basin. *Journal of Geophysical Research: Solid Earth*, *103*(B4), 7187–7210. https://doi.org/10.1029/97JB03536

Zhang, J., & Toksöz, M. N. (1998). Nonlinear refraction traveltime tomography. *Geophysics*, *63*(5), 1726–1737. https://doi.org/10.1190/1.1444468